

## Supporting Information

### Development of CrNiCo-P/GCN multifunctional robust catalyst for oxygen evolution, electrochemical sensing, and photodegradation of roxarsone†

Shaktivel Manavalan,<sup>a</sup> Pitchaimani Veerakumar,<sup>\*,c,b</sup> Shen-Ming Chen,<sup>\*,a</sup> Naveen Karuppusamy<sup>a</sup>

<sup>a</sup>Department of Chemical Engineering and Biotechnology, National Taipei University of Technology, Taipei 10608, Taiwan

<sup>b</sup>Department of Chemistry, National Taiwan University, No. 1, Roosevelt Road, Section 4, Taipei 10617, Taiwan

<sup>c</sup>Institute of Atomic and Molecular Sciences, Academia Sinica, No. 1, Roosevelt Road, Section 4, Taipei 10617, Taiwan

**\*Corresponding author**

E-mail address: smchen78@ms15.hinet.net (S.-M. Chen)

spveerakumar@gmail.com (P. Veerakumar)

Number of pages: 49

Number of Figures: 38

Number of tables: 10

<b>Entry</b>	<b>Table of Content</b>	<b>Page No</b>
	<i>Chemicals and Electrolyte</i>	<b>S7</b>
	<i>Material Characterization</i>	<b>S7</b>
	<i>Electrochemical Measurement for OER</i>	<b>S8</b>
	<i>Electrochemical Measurement for ROX Sensor</i>	<b>S9</b>
	<i>Real Sample Preparation for ROX Practical Analysis</i>	<b>S10</b>
	<i>Photocatalytic degradation of ROX</i>	<b>S10</b>
	<i>Turn Over Frequency (TOF)</i>	<b>S10</b>
	<i>Determination of Faradaic Efficiency</i>	<b>S11</b>
<b>Fig. S1.</b>	(a) LSV, (b) Tafel curves and (c) Impedance of the CrNi-P, CrCo-P, CrCo-P/GCN, and CrNi-P/GCN in 1.0 M KOH solution for OER with a scan rate of 5 mV s <sup>-1</sup> . The different amount ratio of CrNiCo-P:GCN based (d) LSV, (e) Tafel curves, and (f) Impedance of the 1:2, 1:1, and 1:2, respectively. Inset of (c) and (f) are model of Randles circuit.	<b>S12</b>
<b>Fig. S2.</b>	(a) LSV curves of different amount of Cr loaded in the CrNiCo-P/GCN measured in 1.0 M KOH solution with a scan rate of 5 mV s <sup>-1</sup> .	<b>S13</b>
<b>Fig. S3.</b>	(a) N <sub>2</sub> -adsorption/desorption isotherms and (b) pore diameter distributions of pristine GCN and CrNiCo-P/GCN samples.	<b>S13</b>
<b>Fig. S4.</b>	TGA analysis of pristine GCN and CrNiCo-P/GCN samples.	<b>S14</b>
<b>Fig. S5.</b>	(a,b) FE-SEM images of CrNiCo-P, (c) FE-SEM-EDX elemental mapping of CrNiCo-P and (d) corresponding individual elemental mapping of Cr (yellow), Ni (red), Co (dark blue), P (magenta).	<b>S14</b>
<b>Fig. S6.</b>	(a) HR-TEM STEM-HAADF image of CrNiCo-P/GCN, (b) overall elemental mapping of CrNiCo-P/GCN and corresponding elemental mapping of (c) Cr, (d) Ni, (e) Co, (f) P, (g) C, (h) N.	<b>S15</b>
<b>Fig. S7.</b>	(a) The HR-TEM dark image indicating the TEM-EDS line scan	<b>S15</b>

position and the spectrum of representative line scans of (b) Cr, (c) Ni, (d) Co, (e) C, (f) N, and (g) P.

- Fig. S8.** High-resolution XPS spectrum of C 1s for pure GCN and CrNiCo-P/GCN **S16**
- Fig. S9.** The different scan rates performance of (a) NiCo-P, (b) CrNiCo-P, and (c) CrNiCo-P/GCN. **S17**
- Fig. S10.** (a-c) CV profiles of CrCo-P and (b-d) CrCo-P/GCN showing the area of redox features considered for the calculation of number of surface active sites. **S18**
- Fig. S11.** (a-c) CV profiles of CrNi-P and (b-d) CrNi-P/GCN showing the area of redox features considered for the calculation of number of surface active sites. **S19**
- Fig. S12.** (a-c) CV profiles of NiCo-P and (b-d) NiCo-P/GCN showing the area of redox features considered for the calculation of number of surface active sites. **S20**
- Fig. S13.** (a-c) CV profiles of CrNiCo-P and (b-d) CrNiCo-P/GCN showing the area of redox features considered for the calculation of number of surface active sites. **S21**
- Fig. S14.** CV curves of ferricyanide-ferrocyanide redox couple for the calculation of stable “collection efficiency (N)” at CrNiCo-P/GCN RDGE in 0.1 M KCl with 5 mM  $[\text{Fe}(\text{CN})_6]^{3-/4-}$  at a scan rate of 10  $\text{mV s}^{-1}$  with rotating speed from 200–2400 rpm. The ring potential was set at 0.23 V vs. Hg/HgO. The N was calculated to be  $0.33 \pm 0.01$  using equation of  $N = -I_R/I_D$  (the ring ( $I_R$ ) and disk ( $I_D$ ) currents in unit of mA). **S22**
- Fig. S15.** Determination of Faradaic efficiency of oxygen evolution reaction on CrNiCo-P/GCN RDGE in 1 M KOH at a rotating rate of 1600 rpm. The disk and ring currents, and the Faradaic efficiency of RDGE are plotted *versus* applied disk potential. The ring potential is set at 0.32 V vs. RHE. **S22**
- Fig. S16.** Liquid FT-IR spectrum of before and after OER long-term stability **S23**

of CrNiCo-P/GCN.

- Fig. S17.** FE-SEM images of CrNiCo-P/GCN: (a) Before OER long-term stability with corresponding FE-SEM-EDX elemental mapping of (a<sub>1</sub>-a<sub>8</sub>) Mix, Cr, Ni, Co, P, C, N, and O. (b) After OER long-term stability with corresponding FE-SEM-EDX elemental mapping of (b<sub>1</sub>-b<sub>8</sub>) Mix, Cr, Ni, Co, P, C, N, and O. **S24**
- Fig. S18.** XPS spectrum of before and after OER long-term stability of CrNiCo-P/GCN: (a) overall survey, and high-resolution of (b) Ni 2p, (c) Co 2p, (d) P 2p, (e) Cr 2p, (f) N 1s, (g) C 1s, (h) O 1s. **S25**
- Fig. S19.** (a) CV curves of various amount of loading CrNiCo-P/GCN catalyst on the electrode and (b) corresponding bar chart diagram of peak current versus catalyst loading. **S26**
- Fig. S20.** Dependence calibration plot of peak current response (green) and peak potential (blue) of ROX (0.03 mM) against various pH value (3–9). **S26**
- Fig. S21.** (a) Live Photos of 0.03 mM ROX without catalyst at pH ranges such as 3.0, 5.0, 7.0 and 9.0 and (b) Corresponding UV spectra. **S27**
- Fig. S22.** Comparison of CV curves of as-prepared catalysts modified GCEs measured in 0.1 mM of ROX. **S28**
- Fig. S23.** CV curves of different scan rate (20–380 mV s<sup>-1</sup>) of CrNiCo-P/GCN/GCE in 0.1 mM of ROX. **S29**
- Fig. S24.** Chronoamperometry response of various concentration of ROX (0.025–0.125 mM) at the CrNiCo-P/GCN. **S29**
- Fig. S25.** (a) Charge transfer properties of bare GCE, NiCo-P, CrNiCo-P, GCN, and CrNiCo-P/GCN modified GCEs (inset: equivalent circuit model), (b) corresponding linear fitting of  $Z'$  versus  $\omega^{-1/2}$  in the low-frequency region. **S30**
- Fig. S26.** (a) CV curves of Bare GCE, GCN, NiCo-P, NiCo-P/GCN, CrNiCo-P, and CrNiCo-P/GCN modified GCE measured in 0.1 M KCl with 5 mM FC/FC<sup>+</sup> at a scan rate of 50 mV/s and (b) the corresponding energy level diagrams. **S30**

- Fig. S27.** (a) Stability test for 14 days in presence of ROX (0.1 mM), (b) S31  
Reproducibility of the GCE at 6 independent measurements in  
presence of ROX (0.1 mM), (c) Repeatability of the sensor for 0.1  
mM of ROX at CrNiCo-P/GCN/GCE, respectively, and (d) the bar  
diagram between peak current versus cycle runs. All experiments  
done in 0.1M PB (pH 5.0) at scan rate of 50 mV s<sup>-1</sup>.
- Fig. S28.** (a) Consecutive 100 CV cycles of ROX (0.1 mM) in 0.1M PB (pH S32  
5.0) at scan rate of 50 mV s<sup>-1</sup>.
- Fig. S29.** The FE-SEM images of CrNiCo-P/GCN: (a) Before ROX sensor S33  
stability with corresponding FE-SEM-EDX elemental mapping of  
(a<sub>1</sub>-a<sub>8</sub>) Mix, Cr, Ni, Co, P, C, N, and O. (b) After ROX sensor  
stability (0.1 mM) with corresponding FE-SEM-EDX elemental  
mapping of (b<sub>1</sub>-b<sub>8</sub>) Mix, Cr, Ni, Co, P, C, N, and O.
- Fig. S30.** XPS spectrum of before and after ROX sensing long-term stability S34  
of CrNiCo-P/GCN: (a) overall survey, and high-resolution of (b) Ni  
2p, (c) Co 2p, (d) P 2p, (e) Cr 2p, (f) N 1s, (g) C 1s, (h) O 1s.
- Fig. S31.** Practical sensor of ROX (0-0.003 mM) at CrNiCo-P/GCN in (a) S35  
chicken and (b) swine meats.
- Fig. S32.** Liquid FTIR spectrum of before and after reduction of ROX S35  
solution with phosphate buffer (pH 5.0).
- Fig. S33.** UV-Vis absorption spectra for the photodegradation of ROX in the S36  
(a) absence of VL, (b) GCN, and (c) NiCo-P catalysts.
- Fig. S34.** (a,b) UV spectra and (c,d) Tauc plots of GCN and CrNiCo-P/GCN. S37
- Fig. S35.** Photocurrent measurement of GCN and CrNiCo-P/GCN in 0.1 M S38  
NaOH under the UV light wavelength of 365 nm.
- Fig. S36.** The XPS high-resolution spectra of As 3d before photodegradation, S38  
and after photodegradation of ROX in the presence of CrNiCo-  
P/GCN.
- Fig. S37.** The FE-SEM images of CrNiCo-P/GCN: (a) Before S39  
photodegradation stability material of ROX with corresponding FE-

SEM-EDX elemental mapping of (a<sub>1</sub>-a<sub>8</sub>) Mix, Cr, Ni, Co, P, C, N, and O. (b) After photodegradation stability material of ROX with corresponding FE-SEM-EDX elemental mapping of (b<sub>1</sub>-b<sub>8</sub>) Mix, Cr, Ni, Co, P, C, N, and O.

<b>Fig. S38.</b>	XPS spectrum of before and after ROX photodegradation stability of CrNiCo-P/GCN: (a) overall survey, and high-resolution of (b) Ni 2p, (c) Co 2p, (d) P 2p, (e) Cr 2p, (f) N 1s, (g) C 1s, (h) O 1s.	<b>S40</b>
<b>Table S1.</b>	Summary of textural properties of prepared samples	<b>S41</b>
<b>Table S2.</b>	Elemental quantitative results of CrNiCo-P/GCN from HRTEM-EDS.	<b>S41</b>
<b>Table S3.</b>	Elemental results for CrNiCo-P/GCN, CrNiCo-P, NiCo-P, and GCN derived from surface sensitive XPS.	<b>S41</b>
<b>Table S4.</b>	Summary of various catalytic electrodes for OER in 1.0 M KOH.	<b>S42</b>
<b>Table S5.</b>	The Turn Over Frequencies (TOFs) values of synthesized catalysts for OER (at J = 10 mA cm <sup>-1</sup> )	<b>S42</b>
<b>Table S6.</b>	The redox peak potentials and energy levels of prepared catalyst.	<b>S43</b>
<b>Table S7.</b>	Comparison of CrNiCo-P/GCN modified electrode to the previously reported literatures for electrochemical detection of ROX.	<b>S44</b>
<b>Table S8.</b>	Voltammetric determination of ROX in chicken and swine meat samples.	<b>S45</b>
<b>Table S9.</b>	Chemical structure and some properties of ROX used in this study.	<b>S46</b>
<b>Table S10.</b>	Photodegradation performances of ROX over various catalysts.	<b>S47</b>
	<i>References</i>	<b>S47</b>

**Chemicals and Electrolyte.** Ruthenium(IV) oxide hydrate (RuO<sub>2</sub>·H<sub>2</sub>O, 99.9%), chromium(III) chloride hexahydrate (CrCl<sub>3</sub>·6H<sub>2</sub>O, ≥98.0%), nickel(II) nitrate hexahydrate (Ni(NO<sub>3</sub>)<sub>2</sub>·6H<sub>2</sub>O, 99.99%), cobalt(II) nitrate hexahydrate (Co(NO<sub>3</sub>)<sub>2</sub>·6H<sub>2</sub>O, 99.99%), sodium hypophosphite monohydrate (NaH<sub>2</sub>PO<sub>2</sub>·H<sub>2</sub>O, ≥99.0%) and ethanol (C<sub>2</sub>H<sub>5</sub>OH, 99%), urea (≥99.5%), ammonium

chloride ( $\text{NH}_4\text{Cl}$ , 99.99%) were received from Sigma-Aldrich Ltd. Roxarsone (ROX, purity >99%) was purchased from Alfa Aesar. All chemicals were analytical grade and used without further purification. Chicken and swine meats for real sample practical analysis were purchased from local super market. 1.0 M KOH (pH 14.0) was used as a supporting electrolyte in OER performance. The phosphate buffer (PB; 0.1 M, pH 7.0) supporting electrolyte for ROX sensing was prepared by mixture of 0.0578 M of  $\text{Na}_2\text{HPO}_4 \cdot 7\text{H}_2\text{O}$  and 0.0422 M of  $\text{NaH}_2\text{PO}_4 \cdot \text{H}_2\text{O}$  resulting 0.1 M of Sodium PBS solution. The pH (3–11) value of the solutions was adjusted with 0.5 M  $\text{H}_2\text{SO}_4$  and 1.0 M NaOH. All the electrolytes were  $\text{N}_2$ -gas purged for at least 15 min before the experiments. Millipore system assisted water was used throughout all the experiments.

**Material Characterization.** The XRD patterns were obtained from the XPERT-PRO spectrometer with Cu  $\text{K}\alpha$  radiation ( $\lambda = 1.54 \text{ \AA}$ ) to observe the crystalline nature of the catalysts. The FT-IR was recorded by using the Perkin-Elmer IR spectrometer to acquire the functional group information of the catalysts. The field emission-scanning electron microscopy (FE-SEM) images were captured using the JEOL JSM-7610F attached with an energy dispersive X-ray analyzer (EDX) from Oxford Instruments. The high-resolution transmission electron microscopy (HR-TEM) images were obtained using the Shimadzu JEM-1200 EX at an accelerating voltage of 200 kV. The elemental mapping and high-angle annular dark-field scanning transmission electron microscopy (HAADF-STEM) images were obtained using the Shimadzu JEM-1200 EX bonded with HORIBA EMAX X-ACT. The XPS results were recorded using the Thermo ESCALAB 250 system. The  $\text{N}_2$ -sorption analysis was performed on a Micromeritics, ASAP 2020. Before the  $\text{N}_2$ -sorption measurement, all the samples were degassed at 180 °C for 12 h. Thermogravimetric analysis (TGA) with temperature ramp from 25 to 900 °C at a rate of 10 °C  $\text{min}^{-1}$  in an air atmosphere was used to study the thermal stability of powdered samples. Measurements were

carried out on a NETZSCH TG-209 instrument. The UV-visible absorption spectra were carried out with a Thermo Scientific evolution 220 UV-visible spectrophotometer.

**Electrochemical Measurement for OER.** A conventional three-electrode system combined with a CHI-405a electrochemical workstation (CHI Instruments, USA) was used for the electrochemical measurements at room temperature. A glassy carbon (GC, 0.07 cm<sup>2</sup>) and for long-term stability rotating disk (RDGC, 0.196 cm<sup>2</sup>) electrode coated with catalysts ink was used as the working electrode, and a platinum wire electrode as the counter, and a Hg/HgO electrode (with saturated NaOH solution) was employed as the reference electrodes, respectively. The catalyst ink (6.0 mg mL<sup>-1</sup>) was prepared by blending the catalyst powder (6.0 mg) into the 1.0 mL of solution containing 0.73 mL of ultrapure water, 0.25 mL of isopropanol, and 20 μL of 0.5 wt.% Nafion solution and sonicated to obtain a homogeneous ink. A certain amount of catalyst ink was dropped onto the polished GC (pipetted 10.0 μL) and RDGC (pipetted 28.0 μL) electrode surface, leading to a catalyst loading of ~0.85 mg/cm<sup>2</sup> and oven-dried. All the potentials were calculated according to reversible hydrogen electrode (RHE) scale:  $E(\text{RHE}) = E(\text{Hg/HgO}) + 0.098 + 0.059 \times \text{pH}$ . The LSV and the stability measurements were performed in 1.0 M KOH solution at a scan rate of 5.0 mV s<sup>-1</sup> to obtain the polarization curves. In order to get the original current, no IR compensation was not performed for the LSV curves. The Tafel slope was calculated from polarization curves on the basis of the Tafel equation:  $\eta = a + b \log |j|$ , where  $\eta$  is the overpotential (mV),  $b$  is the Tafel slope, and  $j$  is the current density (mA cm<sup>-2</sup>). Electrochemical impedance spectroscopy (EIS) was carried out by measuring in the frequency range of 10<sup>5</sup>–0.1 Hz at a same configuration at  $\eta = 0.15$  V with an amplitude of 5 mV and the spectrum was shown as Nyquist plot. The electrochemical active surface area (ECSA) of the electrocatalyst was calculated by  $\text{ECSA} = C_{dl}/C_s * S$  where  $C_{dl}$  was estimated from the CV of the double-layer region of electrocatalyst at various scan rates from



5 to 80  $\text{mV s}^{-1}$  in the potential of 1.0–1.2 V vs. RHE,  $C_s$  is general specific capacitance (0.040  $\text{mF cm}^{-2}$  in 1.0 M KOH electrolyte), and  $S$  is the geometric surface area of GCE (0.07  $\text{cm}^{-2}$ ). The capacitive currents of  $\Delta J_{|j_a-j_c|}/2$  at 1.06 V vs. RHE were plotted against the scan rates. The slope of the curves was the double-layer capacitance. As we confirmed that the GCN and bare GC electrodes are contribute very low activity for OER at the current density lower than 10  $\text{mA cm}^{-2}$ , which is meaningless to discuss its performance; therefore, its TOFs values, EIS, and ECSA are not presented in this work.

**Electrochemical Measurement for ROX Sensor.** The electrochemical system was carried out in a three-electrode such as a glassy carbon electrode (GCE, 0.07  $\text{cm}^2$ ) with catalyst as the working, a platinum wire electrode as the counter, and an Ag/AgCl electrode (with saturated KCl) as the reference at room temperature. The CHI instruments used for CV and DPV measurements were CHI-405a and CHI-900 electrochemical workstation from the USA, respectively. The Nyquist plot was obtained by electrochemical impedance spectroscopy (EIS, EIM6ex Zahner, a Germany instrument) under a frequency range of 100–0.01 Hz and amplitude of 5.0 mV at an overpotential of 150 mV in a mixed solution of 5.0 mM  $[\text{Fe}(\text{CN})_6]^{3-/4-}$  and 0.1 M KCl. The catalyst ink (2.0  $\text{mg mL}^{-1}$ ) were prepared by 2.0 mg of the catalyst dispersed into the 1.0 mL DI water without any binder. Subsequently, the mixture was treated with sonication for at least 1 h. The modifying GCE was polished with 0.3  $\mu\text{M}$  of  $\gamma$ -alumina powder and rinsed in the DI water flow. To the polished GCE, an optimized amount of as-prepared electrocatalyst suspension was coated on the electrode surface and dried at 50  $^\circ\text{C}$  for 3 min. The CV and DPV were performed in a potential range from +0.4 to -1.0 V (vs. Ag/AgCl) under  $\text{N}_2$ -purged 0.1 M PB (pH 7.0) solution at a constant scan rate of 50  $\text{mV s}^{-1}$  to obtain the electron transfer curves.

**Real Sample Preparation for ROX Practical Analysis.** A piece of purchased meat (Binjiang market, Taipei city) was cut into 3-4 tiny slices and subsequently, soaked into ultrapure water for a whole day. The meat soaked solution were separated by using Whatman filter paper and then centrifuged at 6000 rpm to settle down the extracted meat substances. From the solution, the supernatant layer was separated to use for experimental purposes.

**Photocatalytic degradation of ROX.** The photocatalytic degradation reactions were carried out using 50 mL of 5.0 mM ROX (pH 7.0) dispersed with 10 mg of as-prepared different photocatalysts. Then the above solution was stirred for 30 min before the light irradiation to accomplish catalyst-ROX (adsorption/desorption) equilibrium. For the photocatalysis reactions, simulated visible-light (VL, xenon lamp, 500 W) irradiation was given from the top of the photocatalytic reactor kept at a 40 cm distance. During the VL irradiation, about 3.0 mL of aliquots were taken every 5 mins, filtered by 0.22  $\mu\text{m}$  sterile syringe filters (PureTech™, Taiwan), and used for further spectrophotometric measurements (Thermo Scientific evolution 220) for the conformations of ROX degradation. Finally, the rate constants for each catalytic reaction with ROX was calculated.

#### **Turn Over Frequency (TOF).**

To investigate the intrinsic oxygen-evolving catalytic activity of synthesized catalysts in this work, the turnover frequencies (TOFs) and surface activities are calculated by the redox feature of the catalysts (Fig. S11-14) as follows.<sup>[S1]</sup>

$$\text{TOF} = j \times NA / F \times n \times \Gamma$$

where,  $j$  is current density taken at 10 mA cm<sup>-2</sup>,  $NA$  is Avogadro number,  $F$  is Faraday constant,  $n$  is number of electrons, and  $\Gamma$  is Surface concentration.

#### **Determination of Faradaic Efficiency**

The Faradaic efficiency of the CrNiCo-P/GCN catalyst for the OER was measured by the RDGE technique and calculated by the following equation:

$$\text{Faradaic efficiency} = j_{\text{R}} \times n_{\text{D}} / j_{\text{D}} \times n_{\text{R}} \times N$$

where,  $j_{\text{R}}$  and  $j_{\text{D}}$  are the ring and disk currents, respectively,  $n_{\text{D}}$  and  $n_{\text{R}}$  are the apparent number of electrons transferred at disk and ring, respectively.  $N$  is the collection efficiency ( $0.33 \pm 0.01$ , Fig. S15).

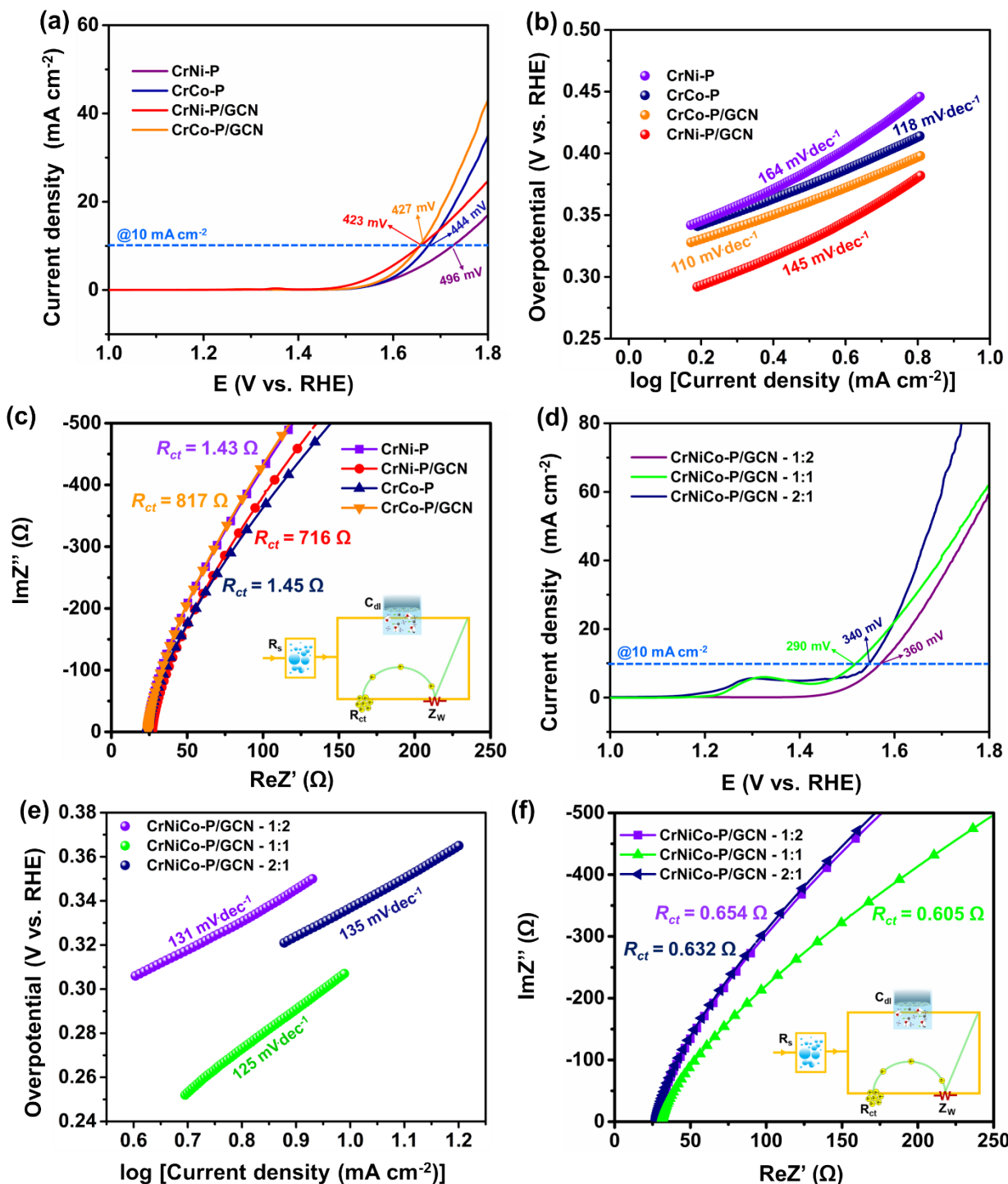


**Fig. S1.** (a) LSV, (b) Tafel curves and (c) Impedance of the CrNi-P, CrCo-P, CrCo-P/GCN, and CrNi-P/GCN in 1.0 M KOH solution for OER with a scan rate of 5 mV s<sup>-1</sup>. The different amount ratio of CrNiCo-P:GCN based (d) LSV, (e) Tafel curves, and (f) Impedance of the 1:2, 1:1, and 1:2, respectively. Inset of (c) and (f) are model of Randles circuit.

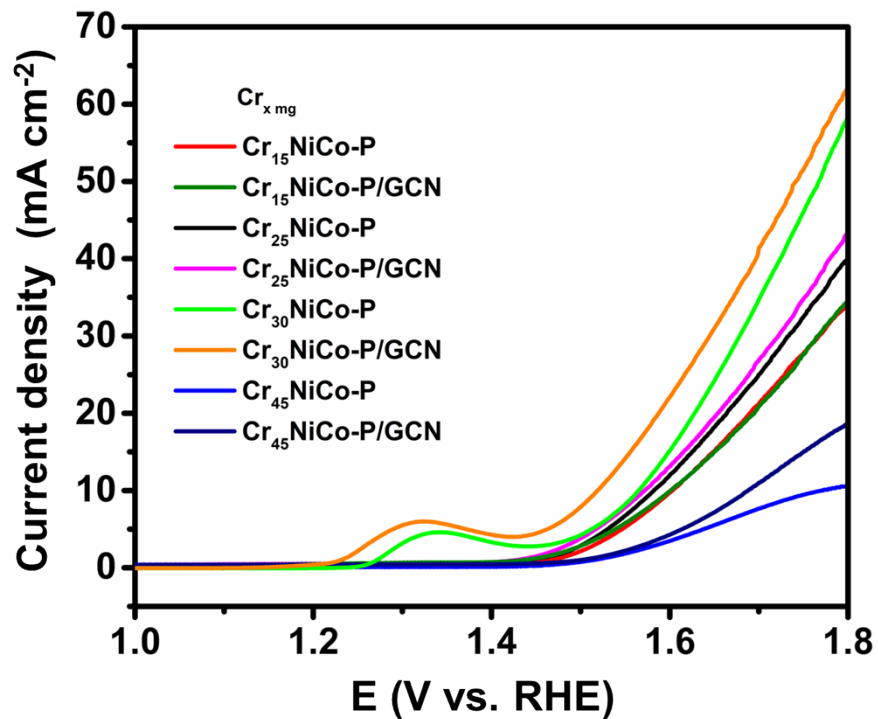


**Fig. S2.** (a) LSV curves of different amount of Cr loaded in the CrNiCo-P/GCN measured in 1.0 M KOH solution with a scan rate of  $5 \text{ mV s}^{-1}$ .

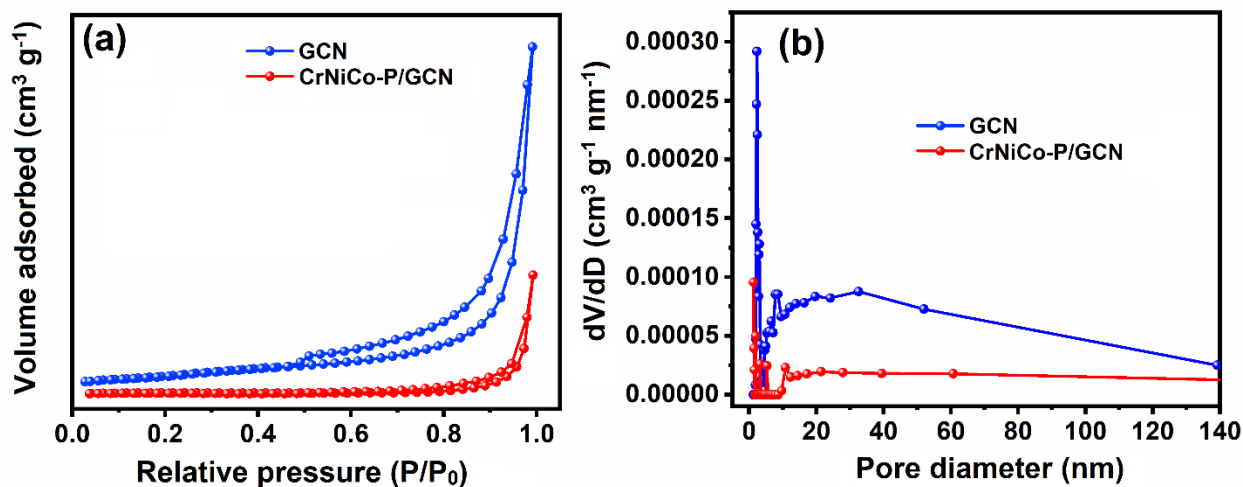


**Fig. S3.** (a)  $\text{N}_2$ -adsorption/desorption isotherms and (b) pore diameter distributions of pristine GCN and CrNiCo-P/GCN samples.

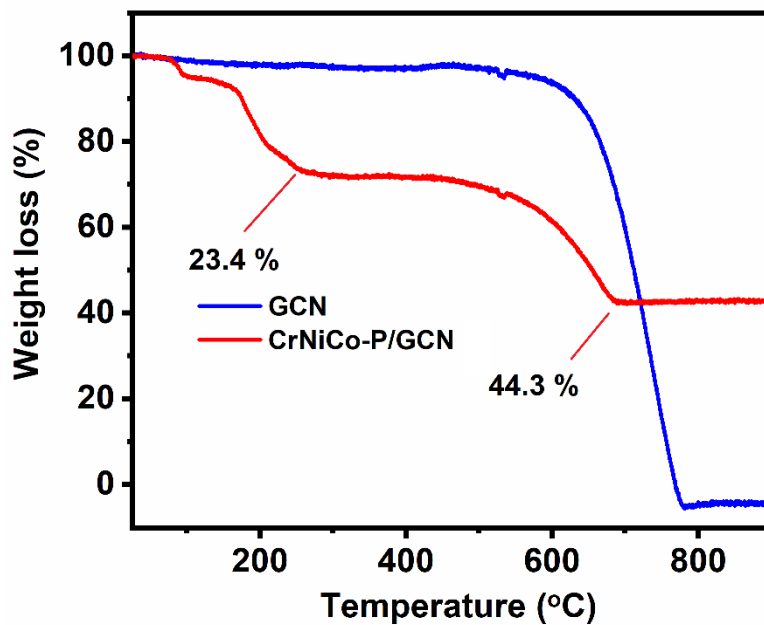


**Fig. S4.** TGA analysis of pristine GCN and CrNiCo-P/GCN samples.

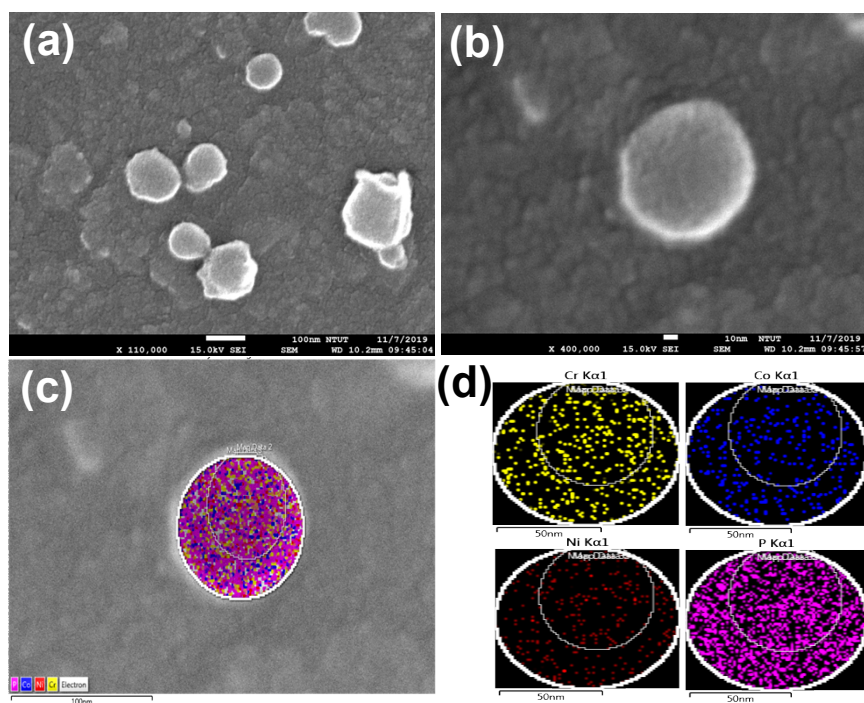


**Fig. S5.** (a,b) FE-SEM images of CrNiCo-P, (c) FE-SEM-EDX elemental mapping of CrNiCo-P and (d) corresponding individual elemental mapping of Cr (yellow), Ni (red), Co (dark blue), P (magenta).

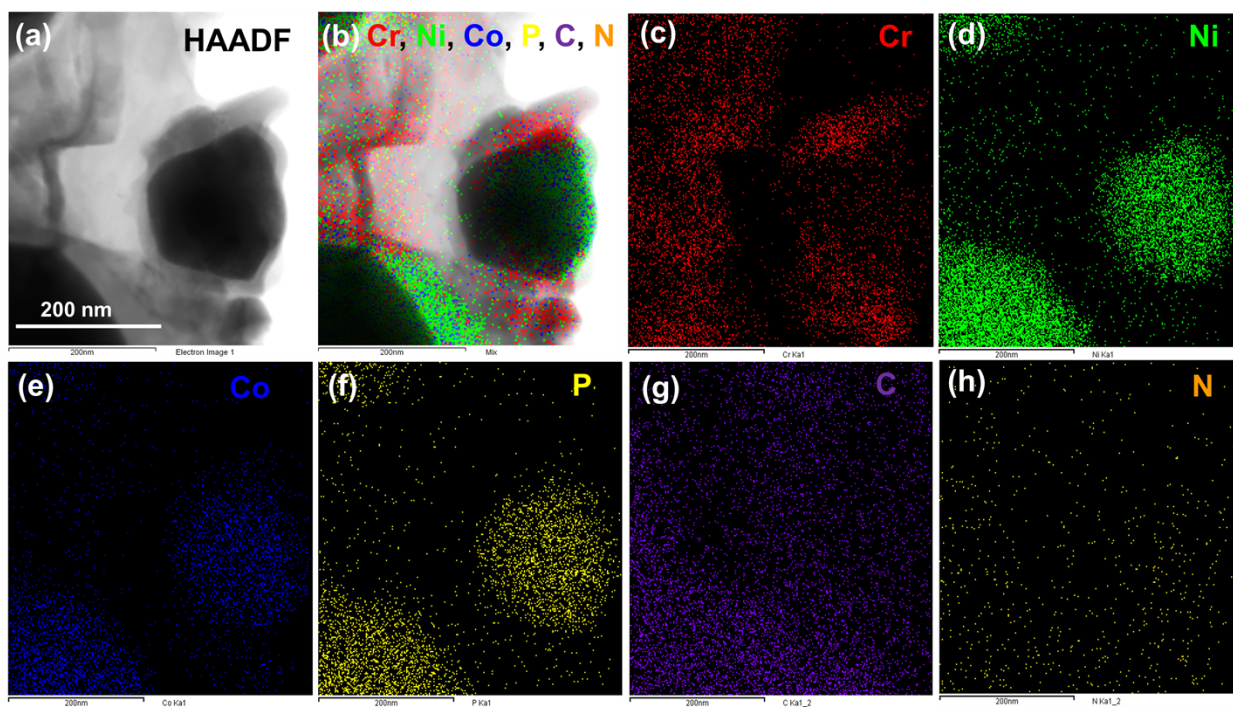


**Fig. S6.** (a) HR-TEM STEM-HAADF image of CrNiCo-P/GCN, (b) overall elemental mapping of CrNiCo-P/GCN and corresponding elemental mapping of (c) Cr, (d) Ni, (e) Co, (f) P, (g) C, (h) N.

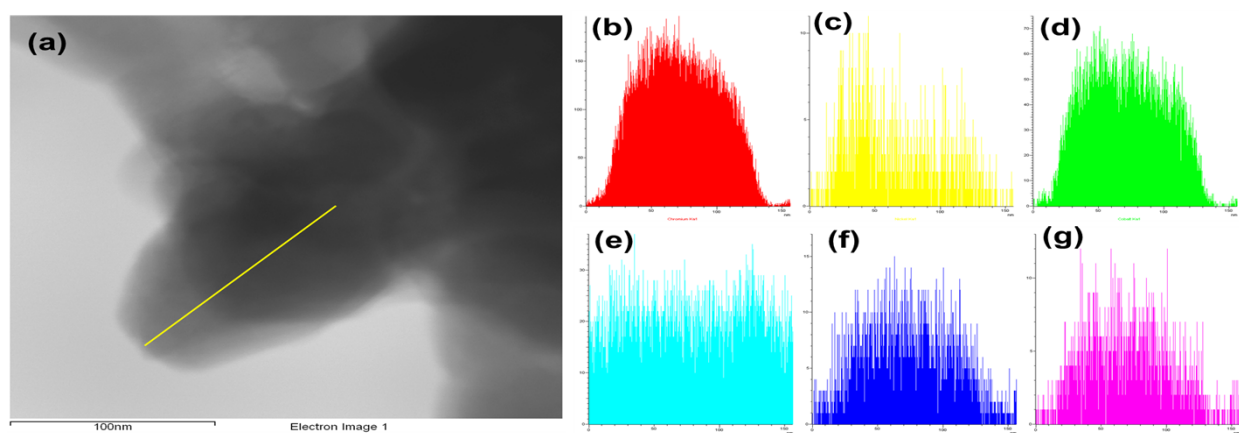


**Fig. S7.** (a) The HR-TEM dark image indicating the TEM-EDS line scan position and the spectrum of representative line scans of (b) Cr, (c) Ni, (d) Co, (e) C, (f) N, and (g) P.

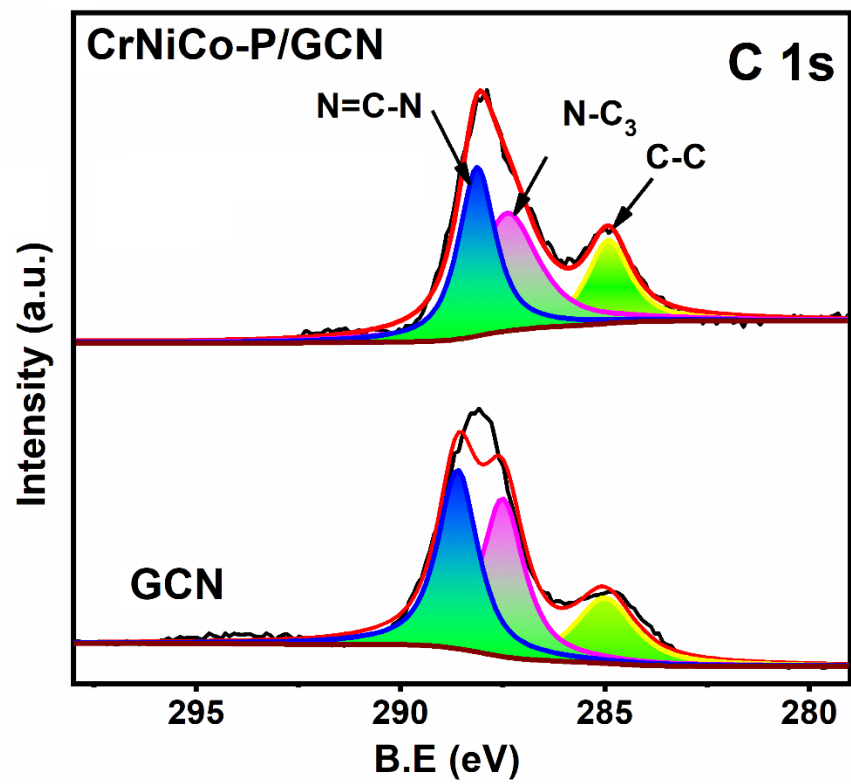


**Fig. S8.** High-resolution XPS spectrum of C 1s for pure GCN and CrNiCo-P/GCN.



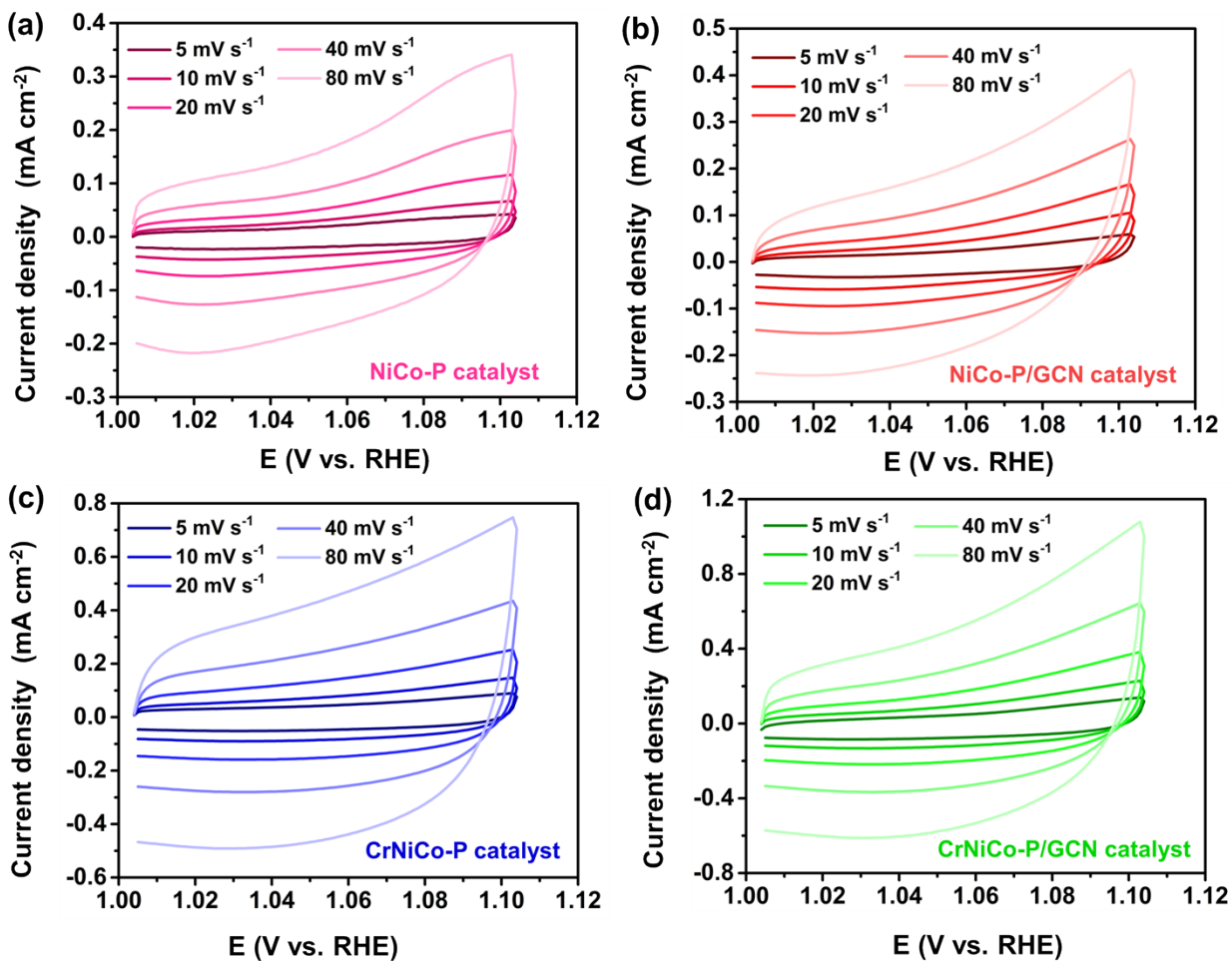


**Fig. S9.** The different scan rates performance of (a) NiCo-P, (b) NiCo-P/GCN, (c) CrNiCo-P, and (d) CrNiCo-P/GCN.

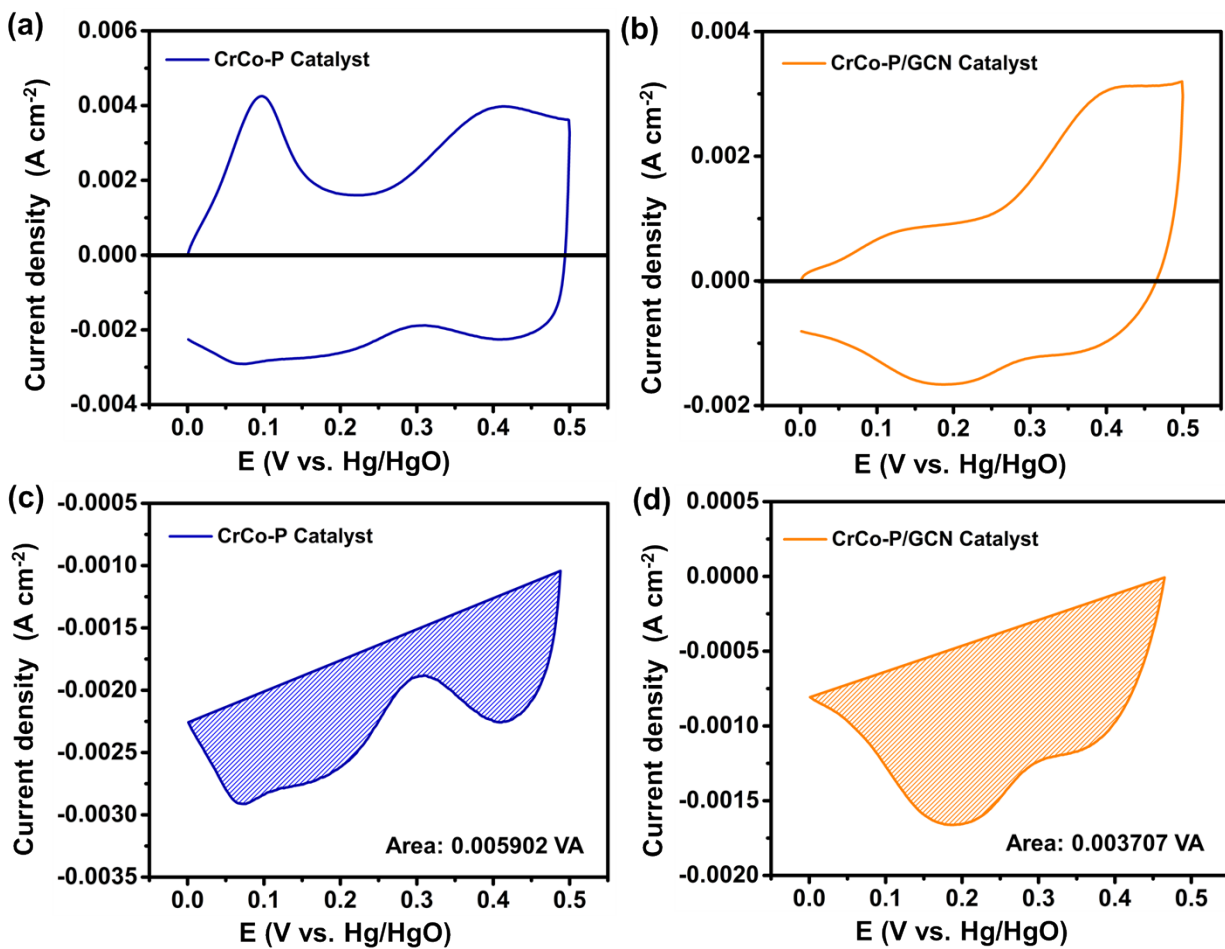


**Fig. S10.** (a-c) CV profiles of CrCo-P and (b-d) CrCo-P/GCN show the area of redox at a scan rate of 300 mV s<sup>-1</sup>, features considered for the calculation of number of surface active sites.

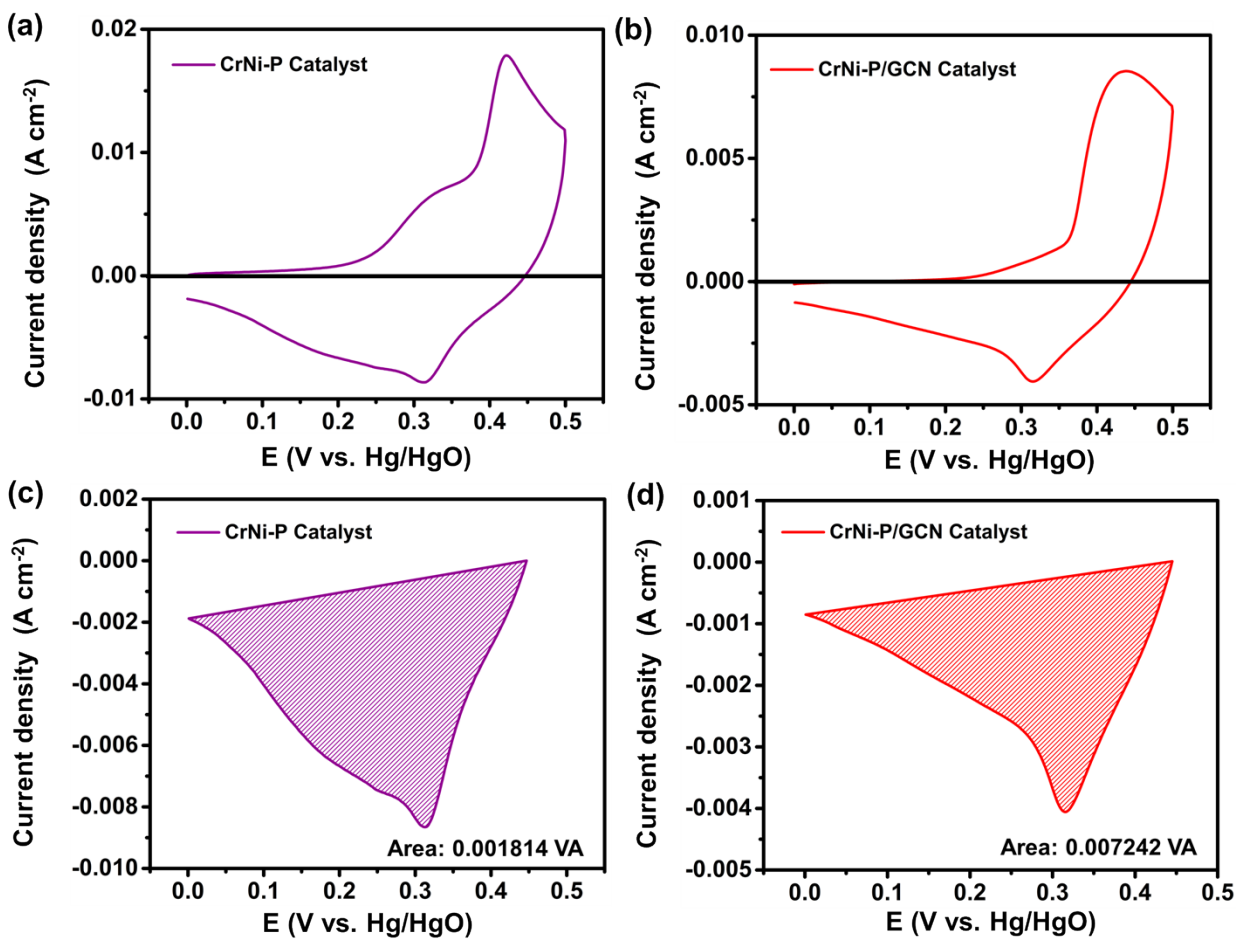


**Fig. S11.** (a-c) CV profiles of CrNi-P and (b-d) CrNi-P/GCN show the area of redox at a scan rate of 300 mV s<sup>-1</sup>, features considered for the calculation of number of surface active sites.

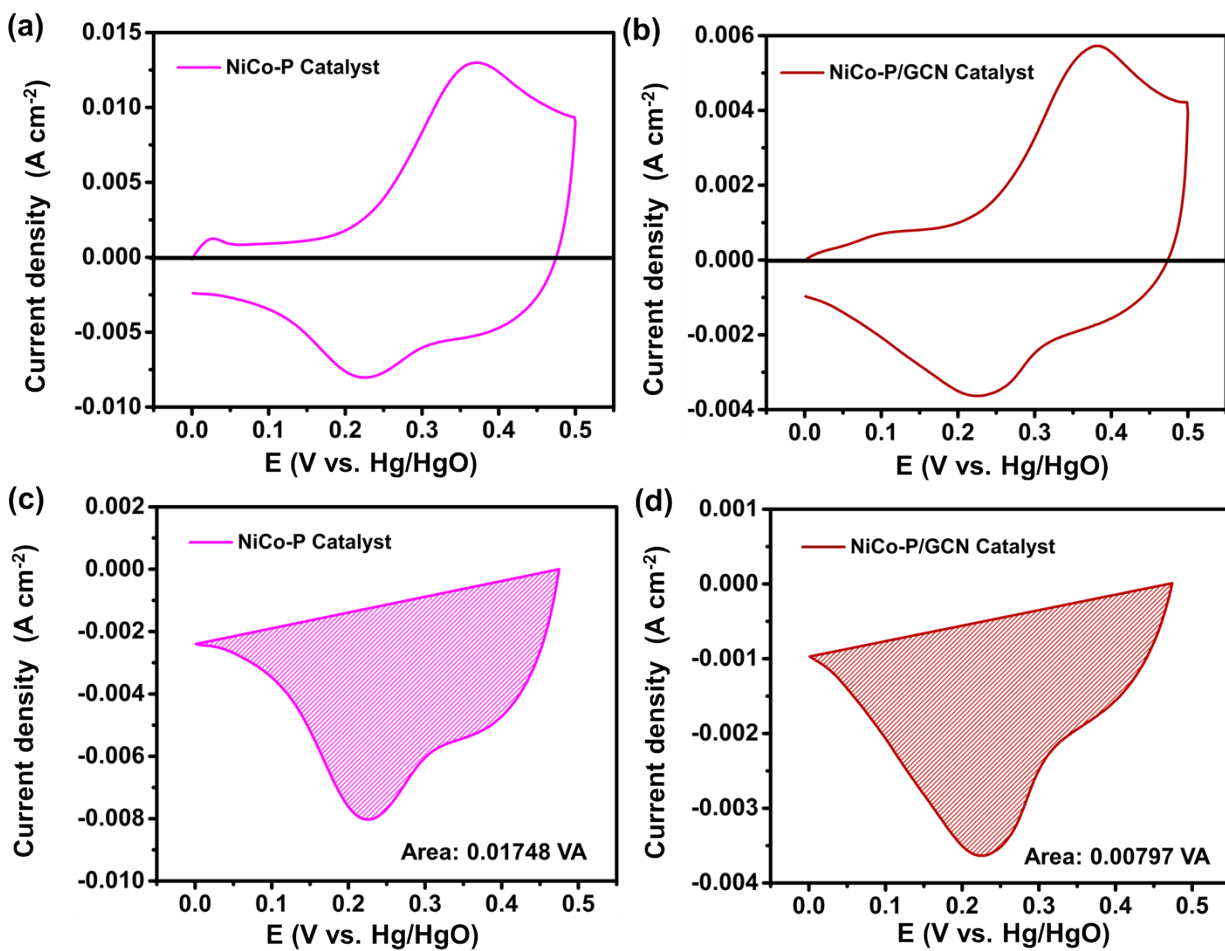


**Fig. S12.** (a-c) CV profiles of NiCo-P and (b-d) NiCo-P/GCN show the area of redox at a scan rate of 300 mV s<sup>-1</sup>, features considered for the calculation of number of surface active sites.

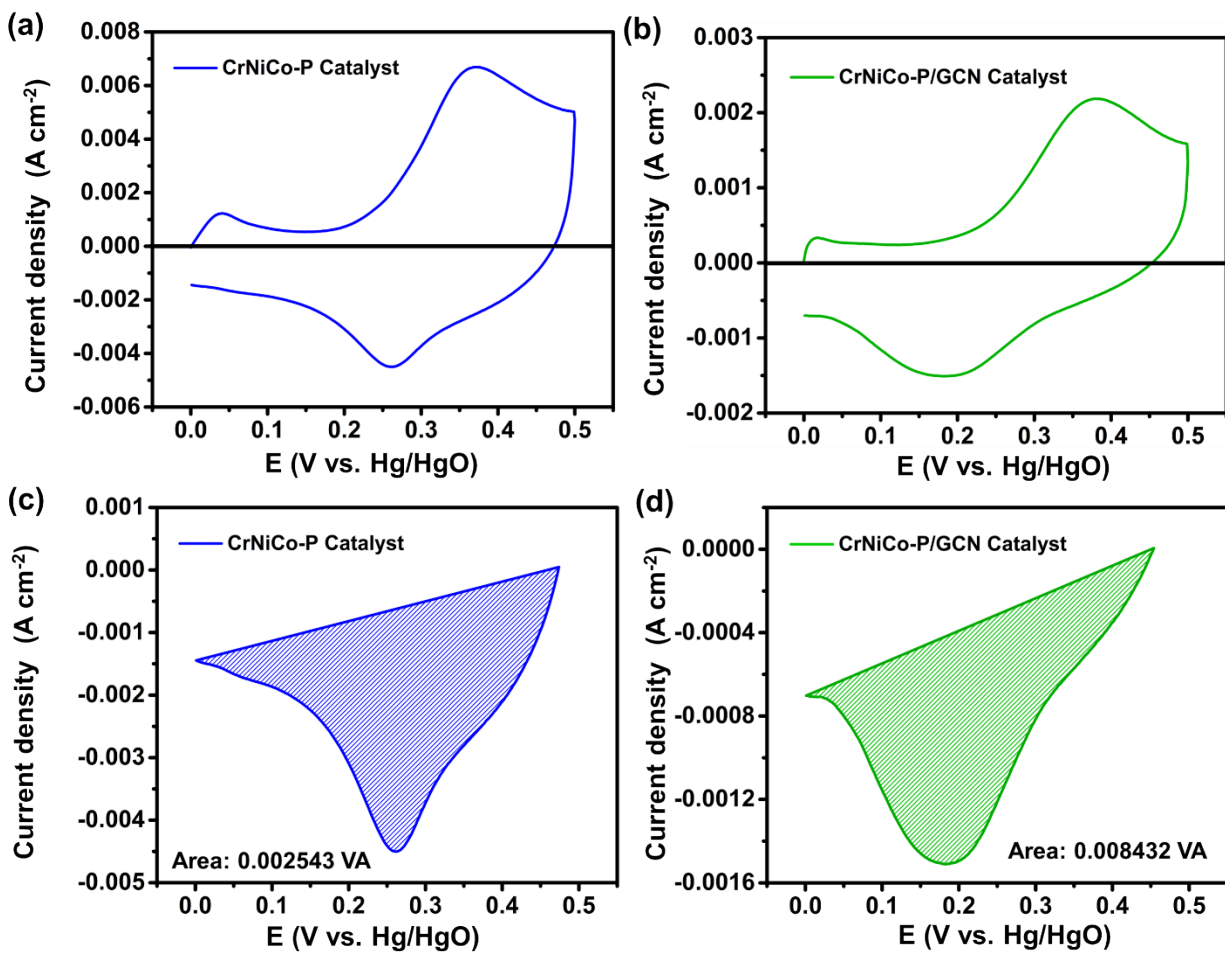


**Fig. S13.** (a-c) CV profiles of CrNiCo-P and (b-d) CrNiCo-P/GCN show the area of redox at a scan rate of  $300 \text{ mV s}^{-1}$ , features considered for the calculation of number of surface active sites.

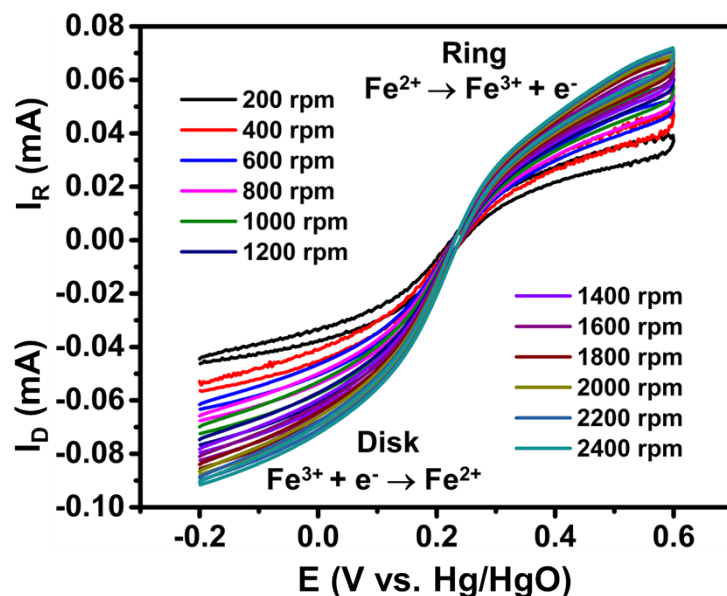


**Fig. S14.** CV curves of ferricyanide-ferrocyanide redox couple for the calculation of stable “collection efficiency (N)” at CrNiCo-P/GCN RDGE in 0.1 M KCl with 5 mM  $[\text{Fe}(\text{CN})_6]^{3-/4-}$  at a scan rate of  $10 \text{ mV s}^{-1}$  with rotating speed from 200–2400 rpm. The ring potential was set at 0.23 V vs. Hg/HgO. The N was calculated to be  $0.33 \pm 0.01$  using equation of  $N = -I_R/I_D$  (the ring ( $I_R$ ) and disk ( $I_D$ ) currents in unit of mA).

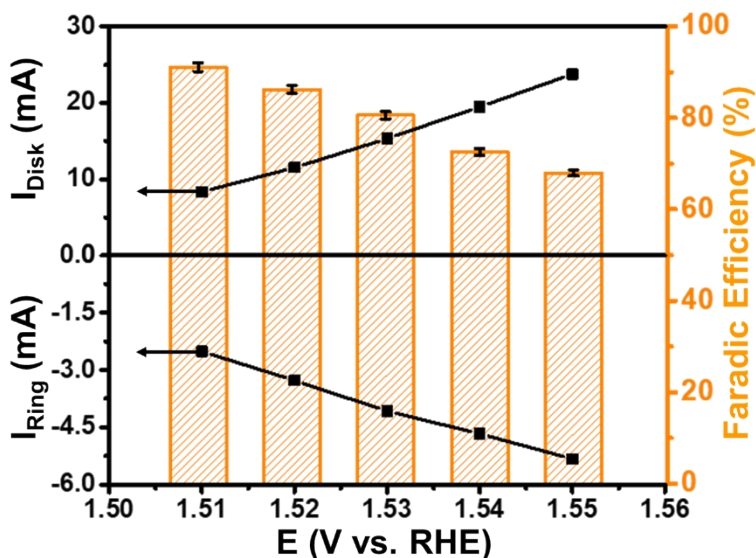


**Fig. S15.** Determination of Faradaic efficiency of oxygen evolution reaction on CrNiCo-P/GCN RDGE in 1 M KOH at a rotating rate of 1600 rpm. The disk and ring currents, and the Faradaic

efficiency of RRDE are plotted *versus* applied disk potential. The ring potential is set at 0.32 V vs. RHE.

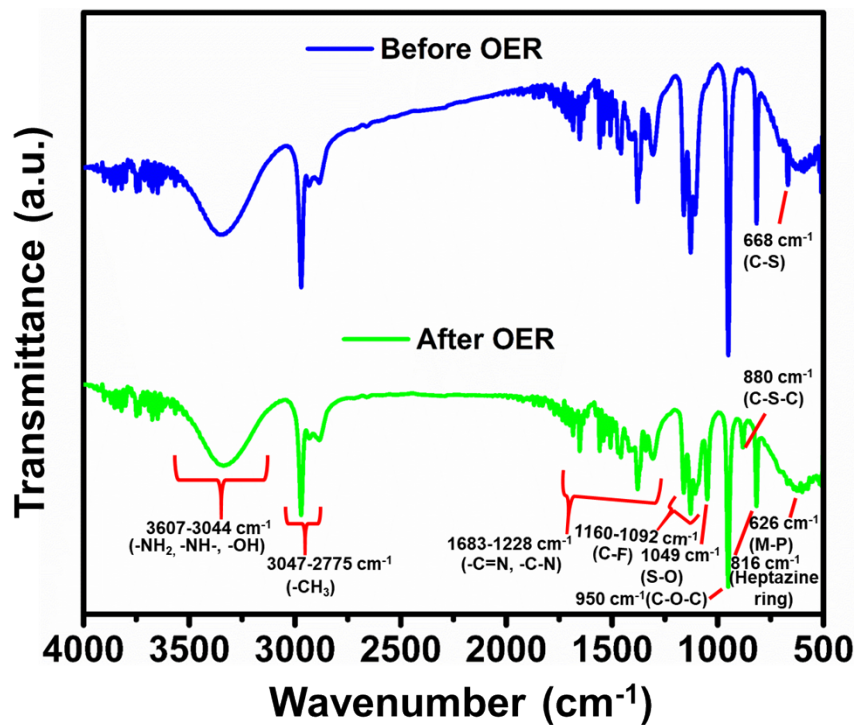


**Fig. S16.** Liquid FT-IR spectrum of before and after OER long-term stability of CrNiCo-P/GCN.

**Note:** The resultant sample contains a Nafion polymer so it may be slightly different from the original.

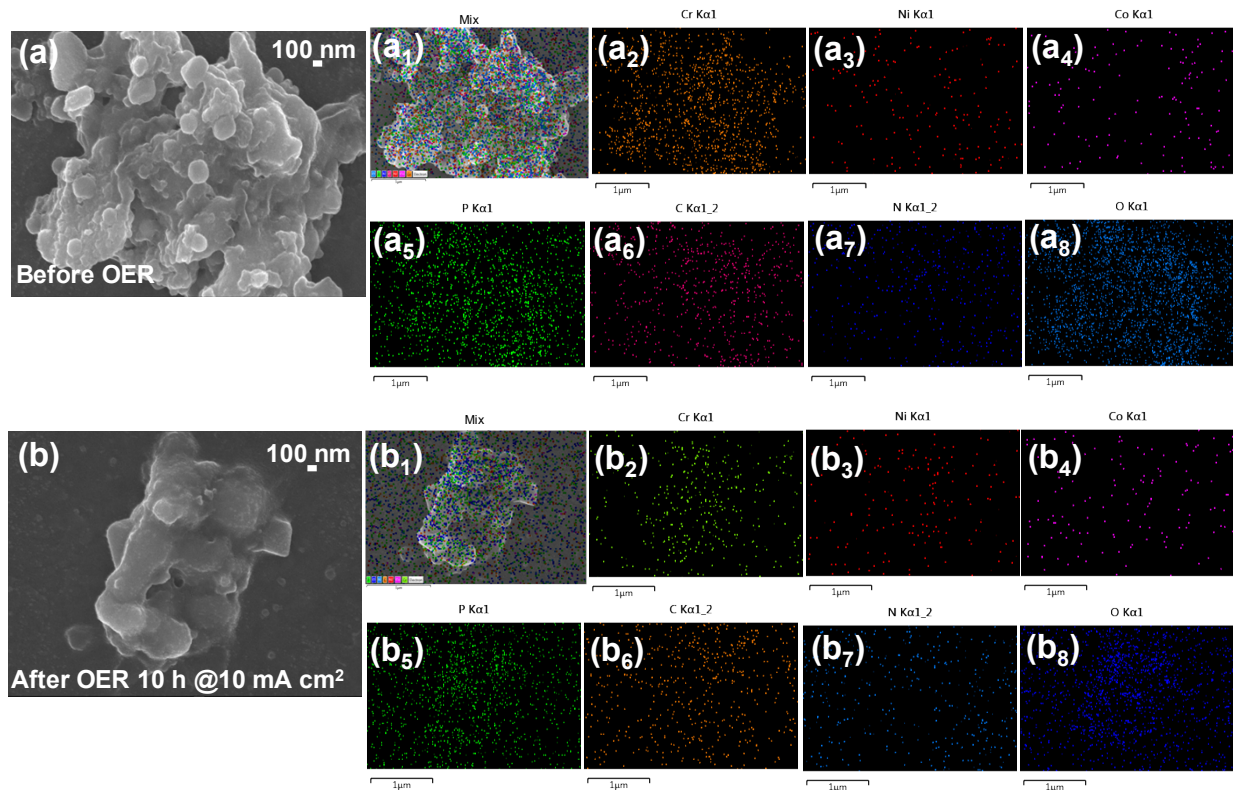


**Fig. S17.** FE-SEM images of CrNiCo-P/GCN: (a) Before OER long-term stability with corresponding FE-SEM-EDX elemental mapping of (a<sub>1</sub>-a<sub>8</sub>) Mix, Cr, Ni, Co, P, C, N, and O. (b) After OER long-term stability with corresponding FE-SEM-EDX elemental mapping of (b<sub>1</sub>-b<sub>8</sub>) Mix, Cr, Ni, Co, P, C, N, and O.

**Note:** The resultant sample contains a Nafion polymer so it may be slightly different from the original.



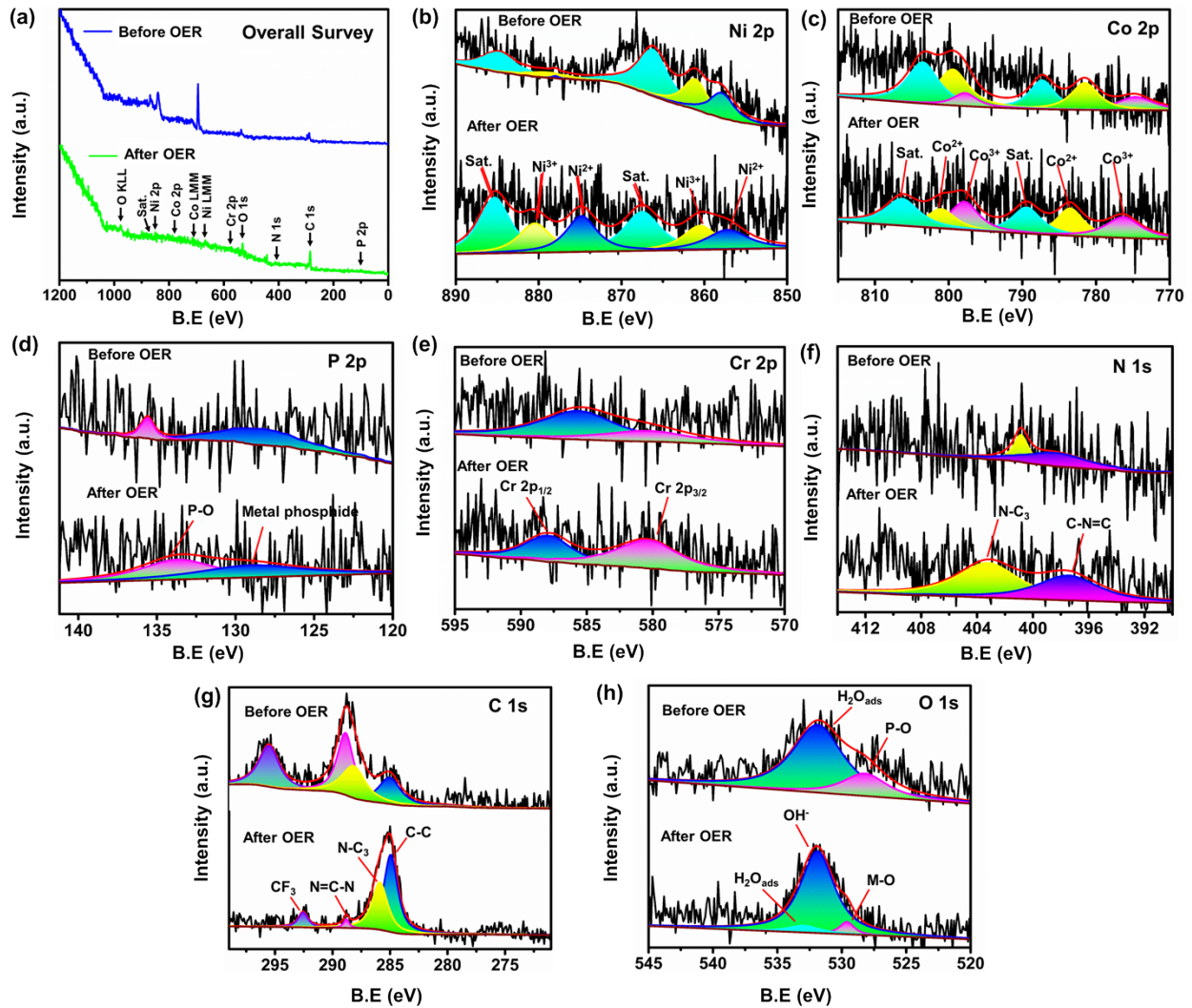


**Fig. S18.** XPS spectrum of before and after OER long-term stability of CrNiCo-P/GCN: (a) overall survey, and high-resolution of (b) Ni 2p, (c) Co 2p, (d) P 2p, (e) Cr 2p, (f) N 1s, (g) C 1s, (h) O 1s.

**Note:** The resultant sample contains a Nafion polymer and the sample were coated on ITO glass for XPS measurement so it may be slightly different from the original.

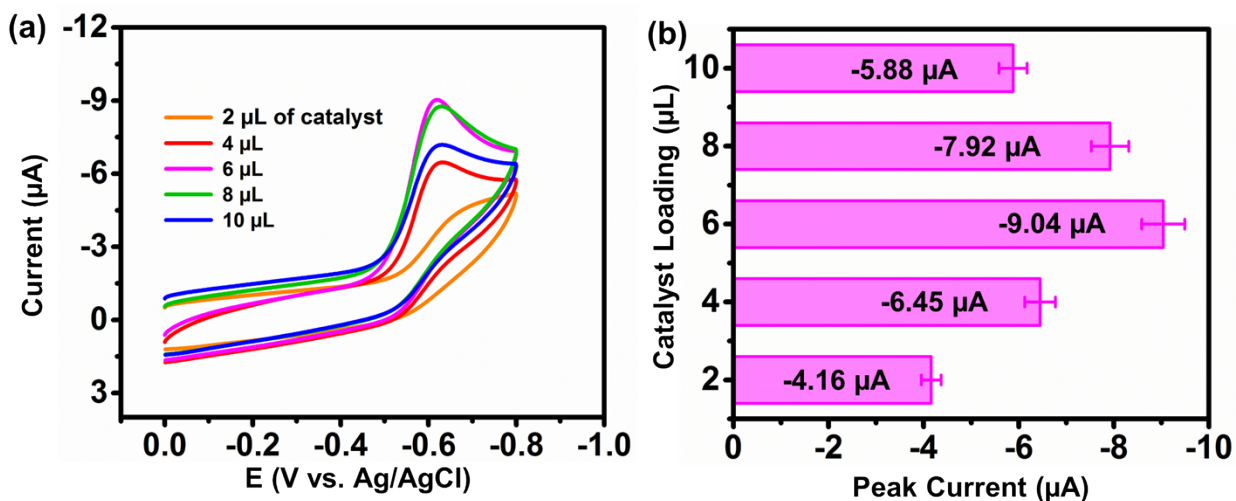


**Fig. S19.** (a) CV curves of various amount of loading CrNiCo-P/GCN catalyst on the electrode and (b) corresponding bar chart diagram of peak current versus catalyst loading.

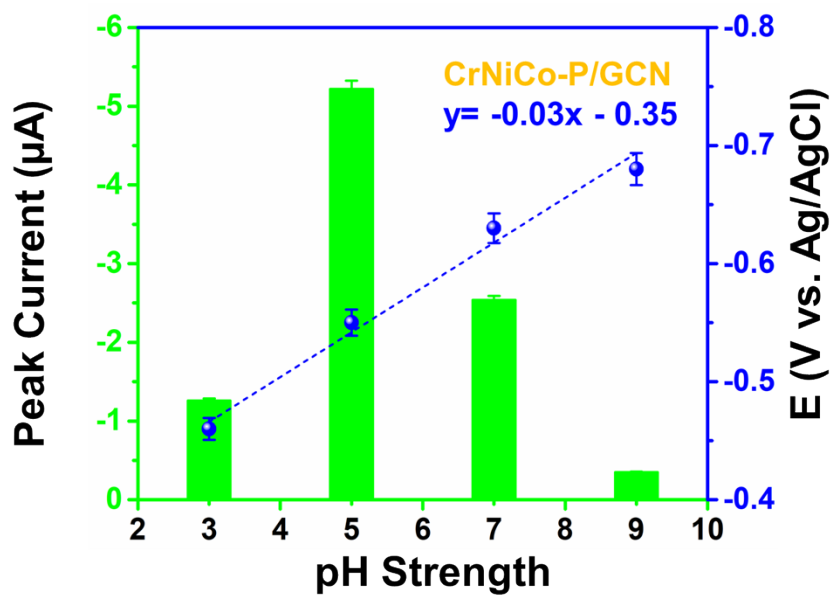


**Fig. S20.** Dependence calibration plot of peak current response (green) and peak potential (blue) of ROX (0.03 mM) against various pH value (3–9).

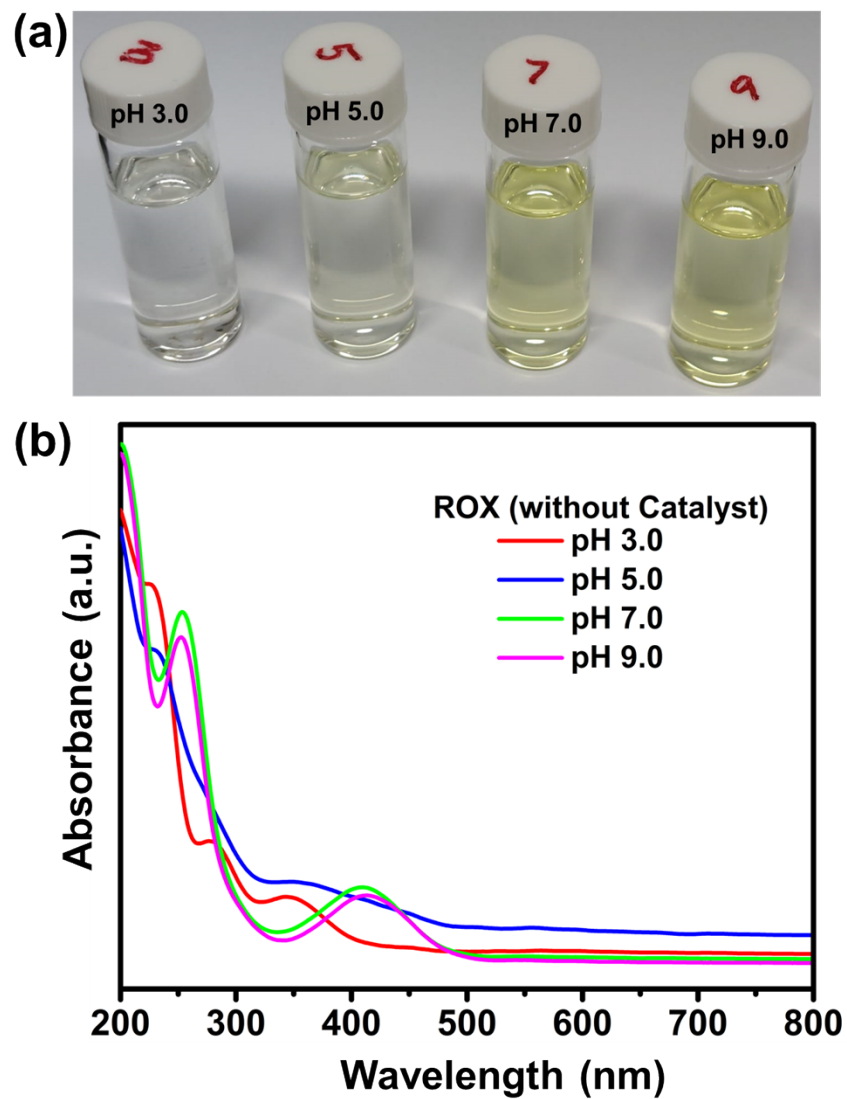


**Fig. S21.** (a) Live Photos of 0.03 mM ROX without catalyst at pH ranges such as 3.0, 5.0, 7.0 and 9.0 and (b) Corresponding UV spectra.

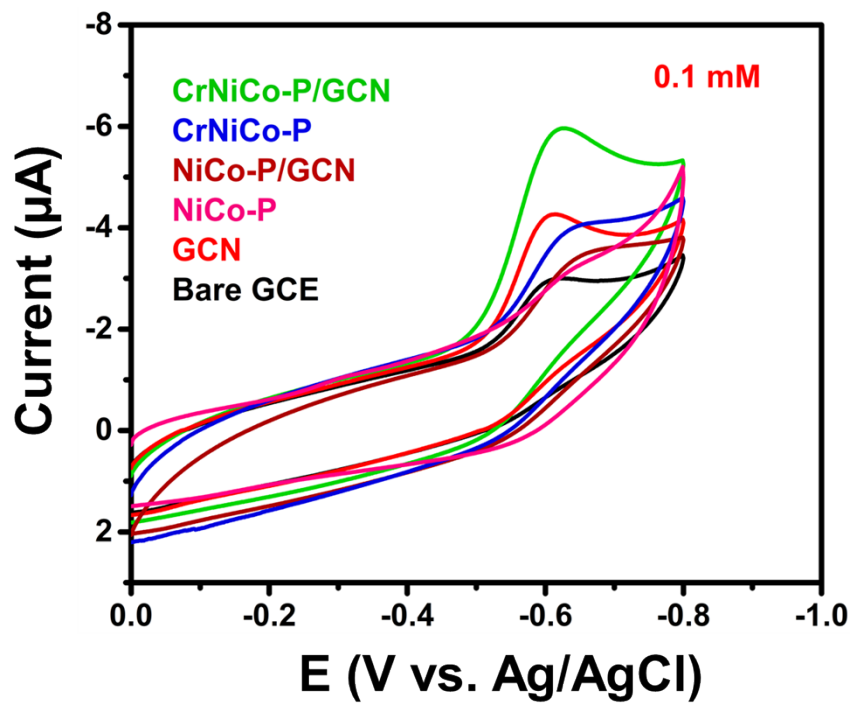


**Fig. S22.** Comparison of CV curves of as-prepared catalysts modified GCEs measured in 0.1 mM of ROX.

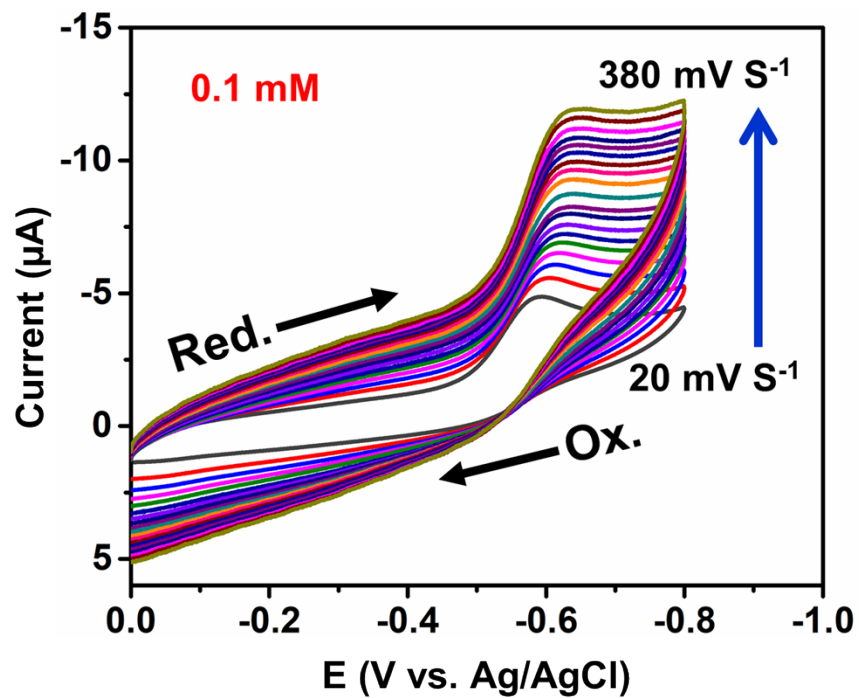


**Fig. S23.** CV curves of different scan rate (20–380  $\text{mV s}^{-1}$ ) of CrNiCo-P/GCN/GCE in 0.1 mM of ROX.

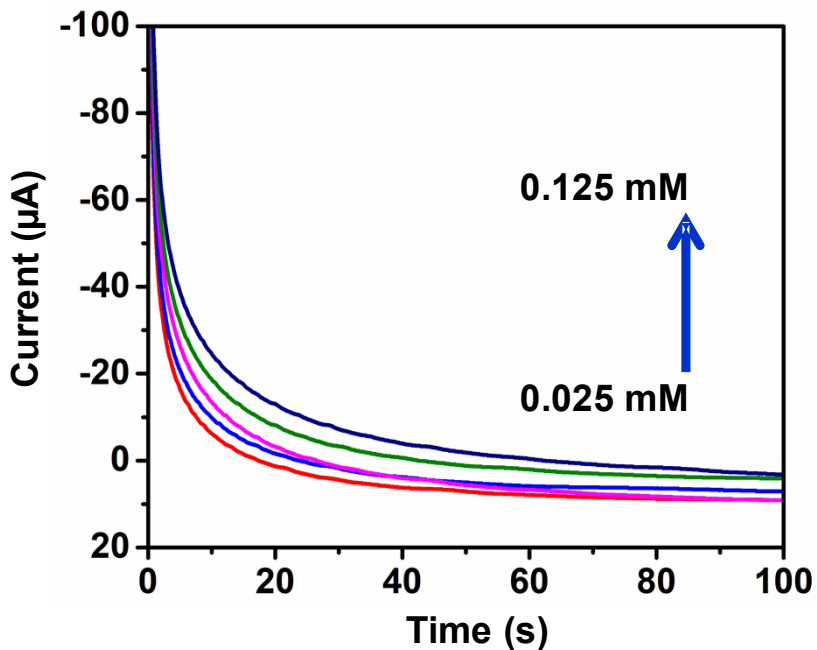


**Fig. S24.** Chronoamperometry response of various concentration of ROX (0.025–0.125 mM) at the CrNiCo-P/GCN.

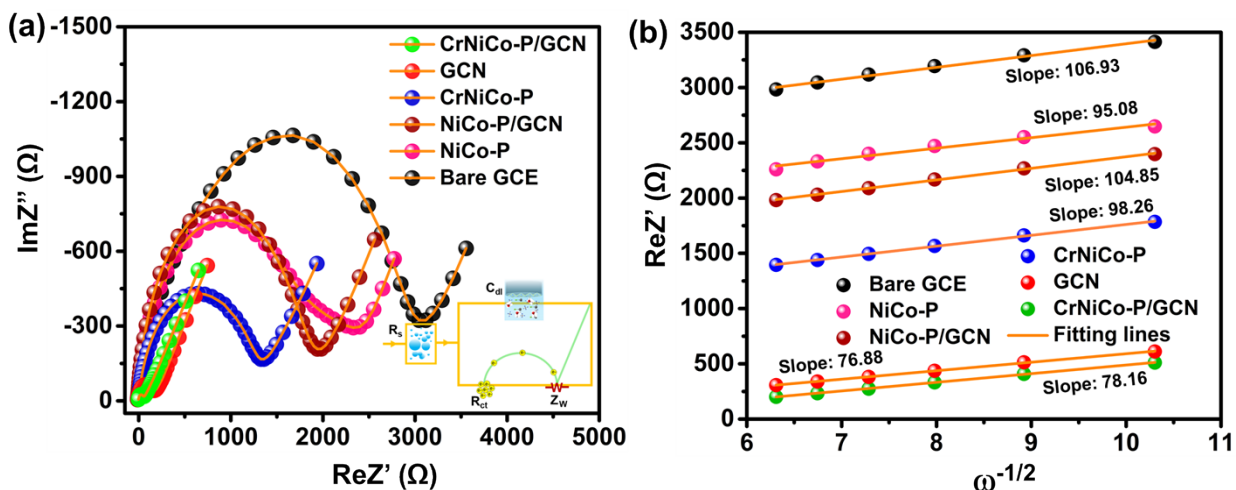


**Fig. S25.** (a) Charge transfer properties of bare GCE, NiCo-P, CrNiCo-P, GCN, and CrNiCo-P/GCN modified GCEs (inset: equivalent circuit model), (b) corresponding linear fitting of  $Z'$  versus  $\omega^{-1/2}$  in the low-frequency region.

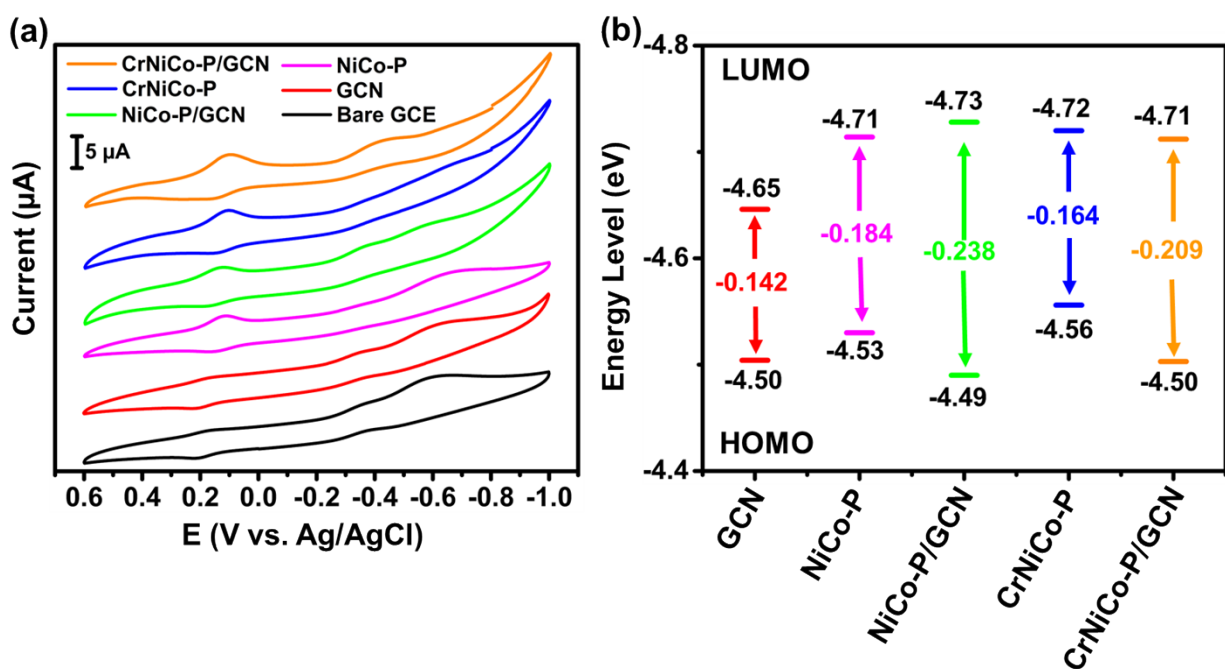


**Fig. S26.** (a) CV curves of Bare GCE, GCN, NiCo-P, NiCo-P/GCN, CrNiCo-P, and CrNiCo-P/GCN modified GCE measured in 0.1 M KCl with 5 mM FC/FC<sup>+</sup> at a scan rate of 50 mV/s and (b) the corresponding energy level diagrams.

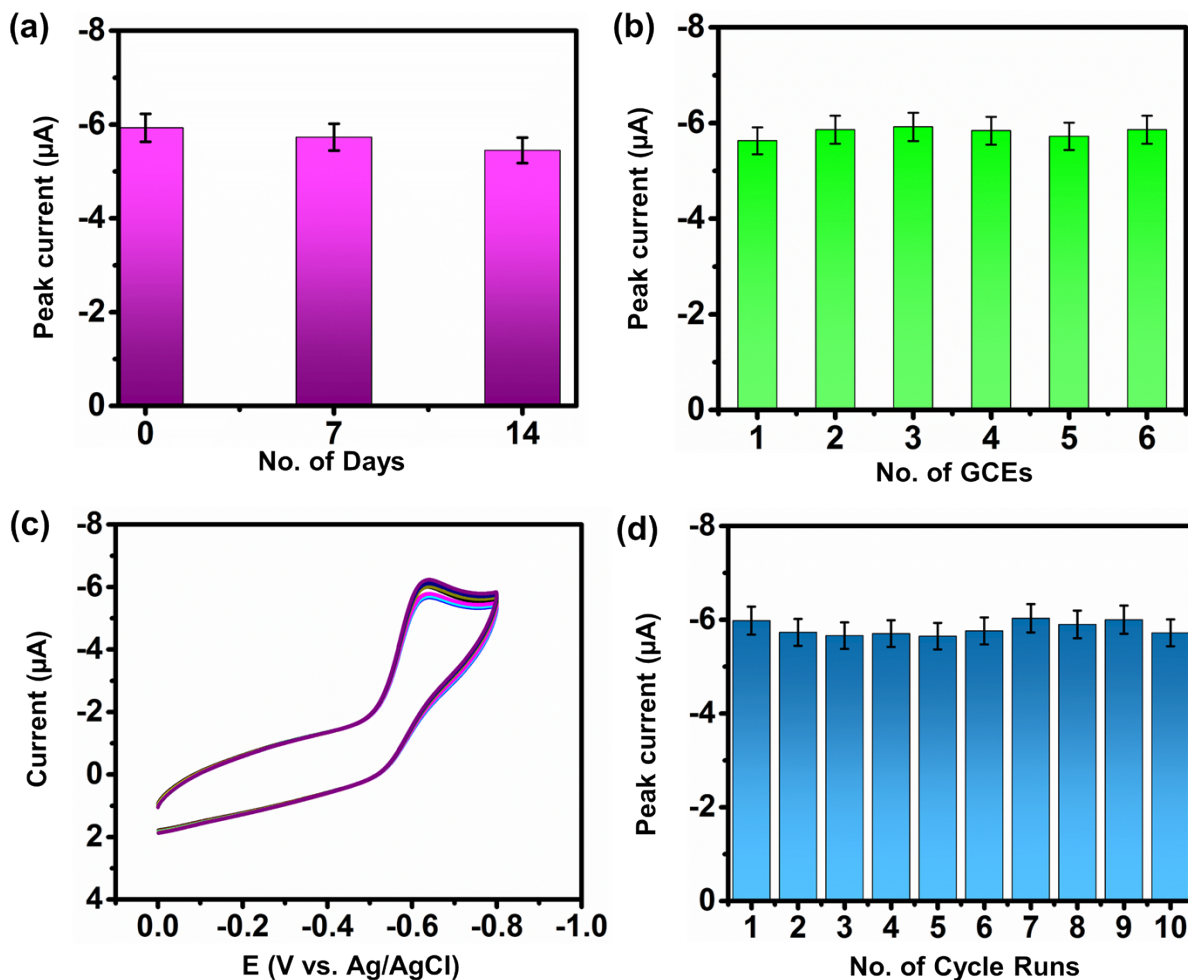


**Fig. S27.** (a) Stability test for 14 days in presence of ROX (0.1 mM), (b) Reproducibility of the GCE at 6 independent measurements in presence of ROX (0.1 mM), (c) Repeatability of the sensor for 0.1 mM of ROX at CrNiCo-P/GCN/GCE, respectively, and (d) the bar diagram between peak current versus cycle runs. All experiments done in 0.1M PB (pH 5.0) at scan rate of  $50 \text{ mV s}^{-1}$ .

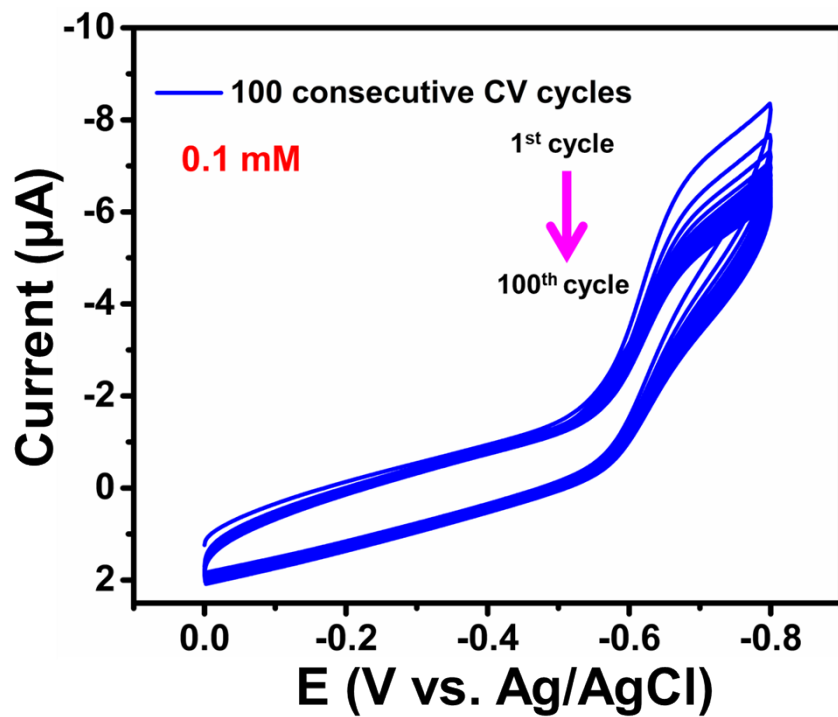


**Fig. S28.** (a) Consecutive 100 CV cycles of ROX (0.1 mM) in 0.1M PB (pH 5.0) at scan rate of  $50 \text{ mV s}^{-1}$ .



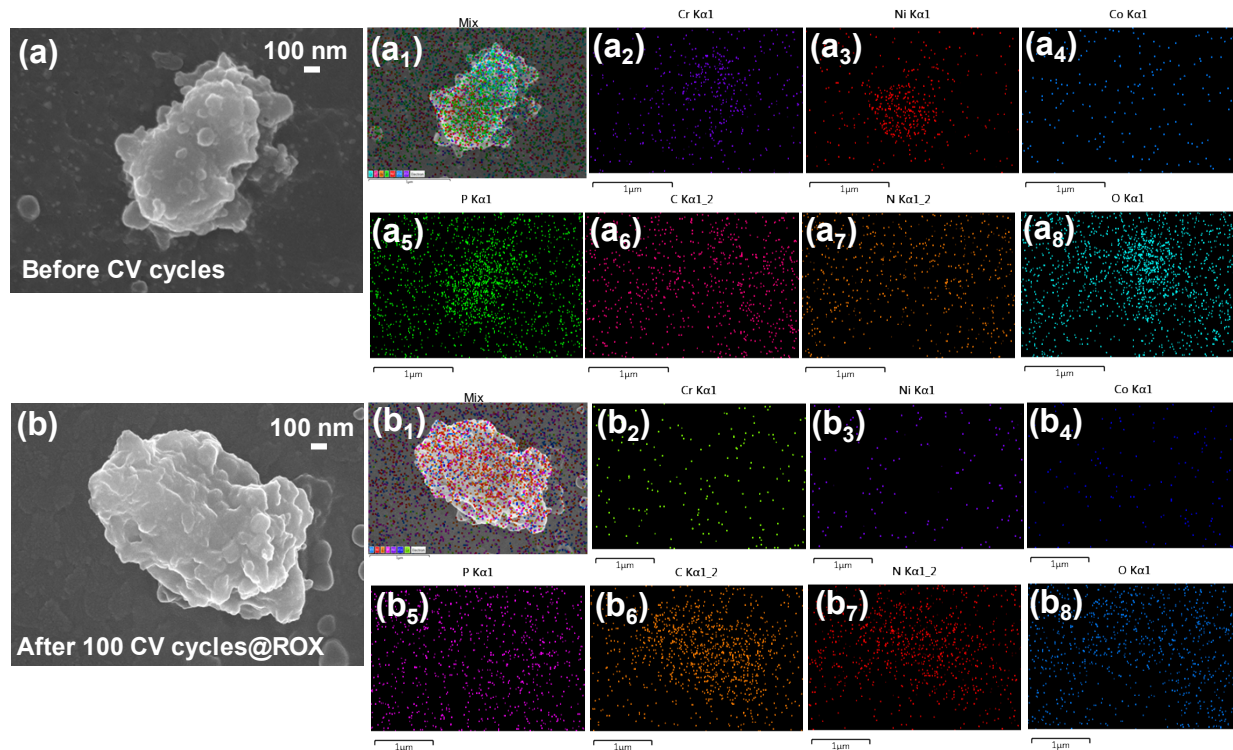


**Fig. S29.** The FE-SEM images of CrNiCo-P/GCN: (a) Before ROX sensor stability with corresponding FE-SEM-EDX elemental mapping of (a<sub>1</sub>-a<sub>8</sub>) Mix, Cr, Ni, Co, P, C, N, and O. (b) After ROX sensor stability (0.1 mM) with corresponding FE-SEM-EDX elemental mapping of (b<sub>1</sub>-b<sub>8</sub>) Mix, Cr, Ni, Co, P, C, N, and O.

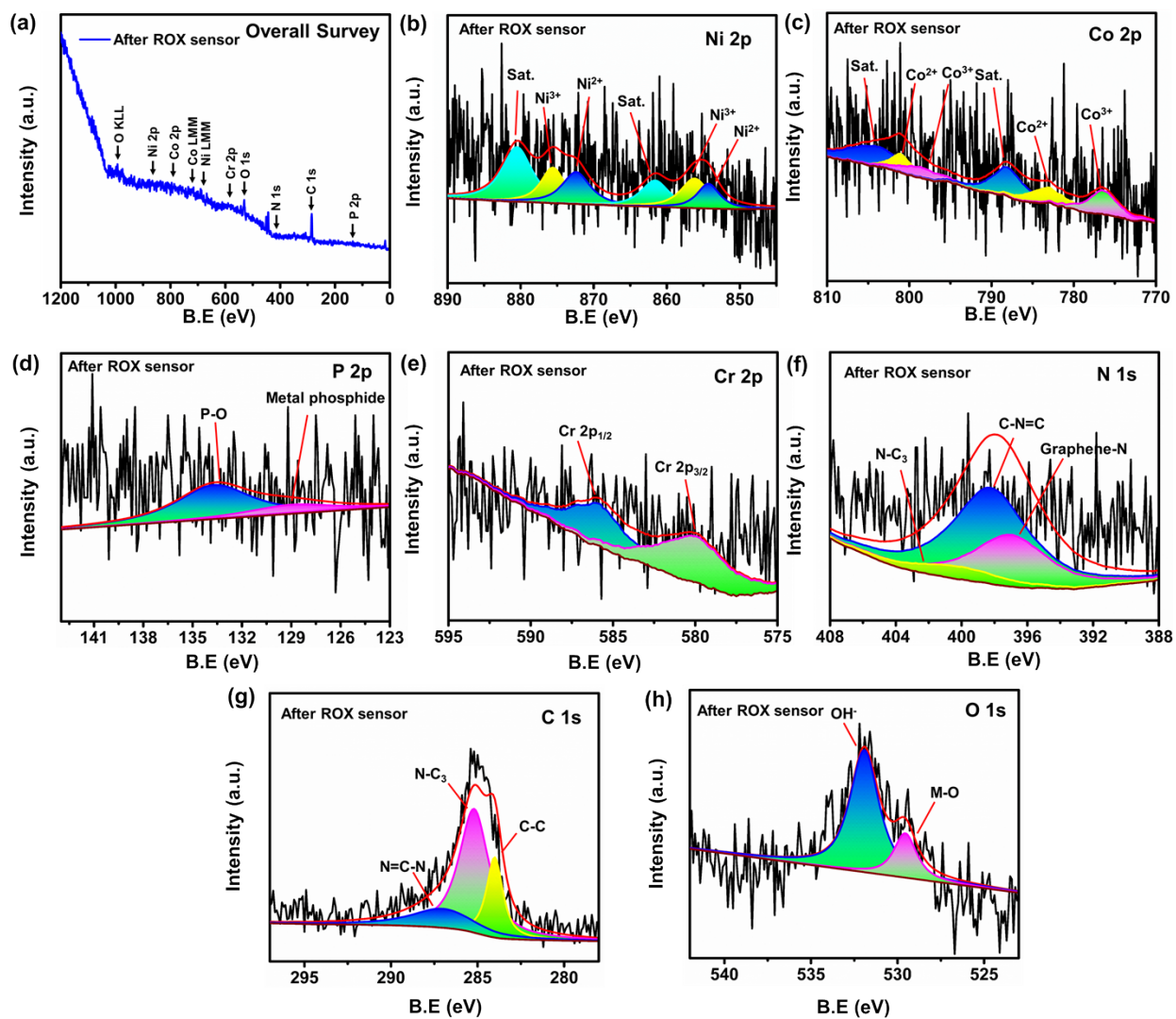


**Fig. S30.** XPS spectrum of before and after ROX sensing long-term stability of CrNiCo-P/GCN: (a) overall survey, and high-resolution of (b) Ni 2p, (c) Co 2p, (d) P 2p, (e) Cr 2p, (f) N 1s, (g) C 1s, (h) O 1s.

**Note:** The resultant sample was coated in ITO glass for XPS measurement so it may be slightly different from the original.

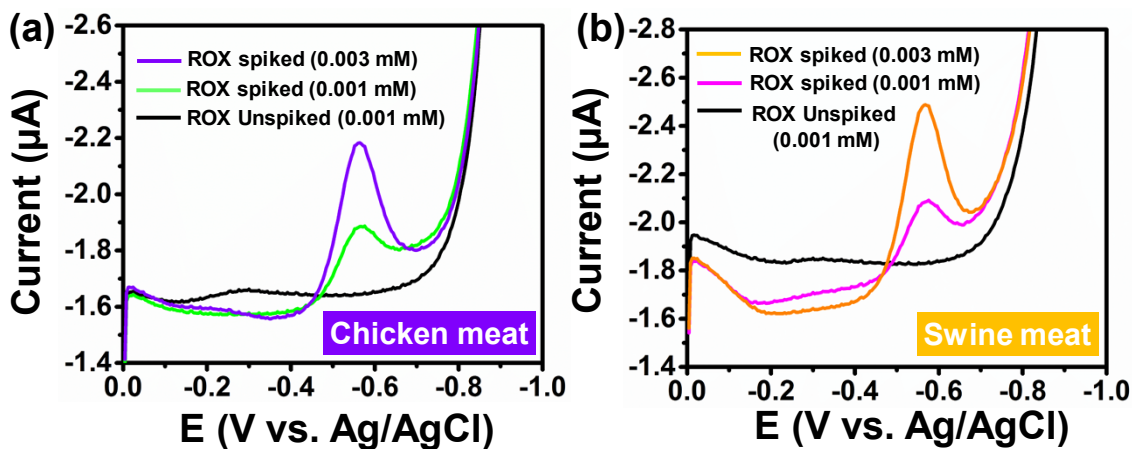


**Fig. S31.** Practical sensor of ROX (0-0.003 mM) at CrNiCo-P/GCN in (a) chicken and (b) swine meats.

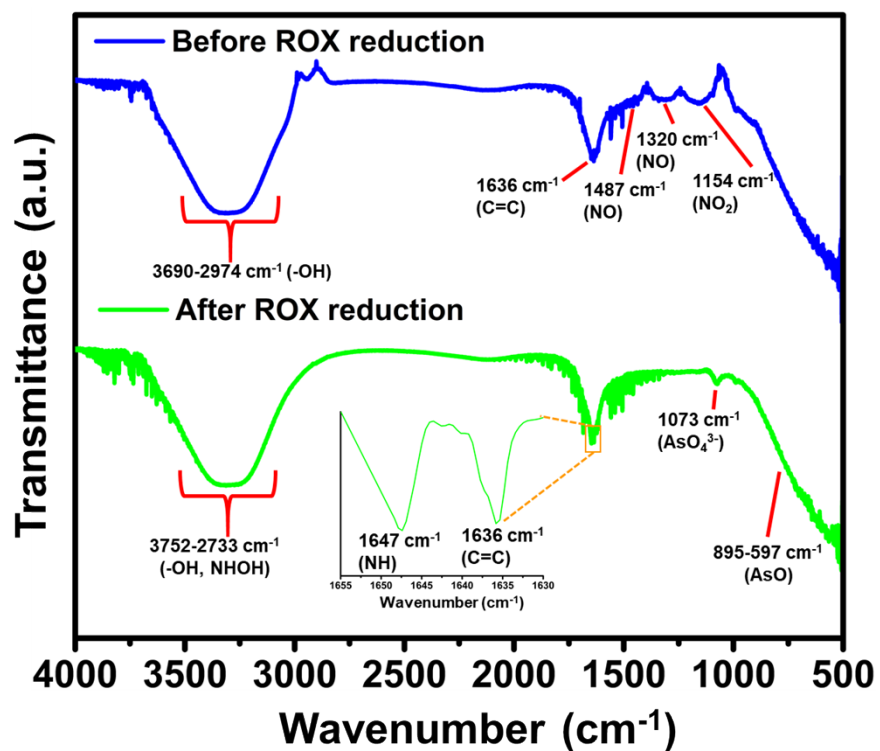


**Fig. S32.** Liquid FTIR spectrum of before and after reduction of ROX solution with phosphate buffer (pH 5.0).

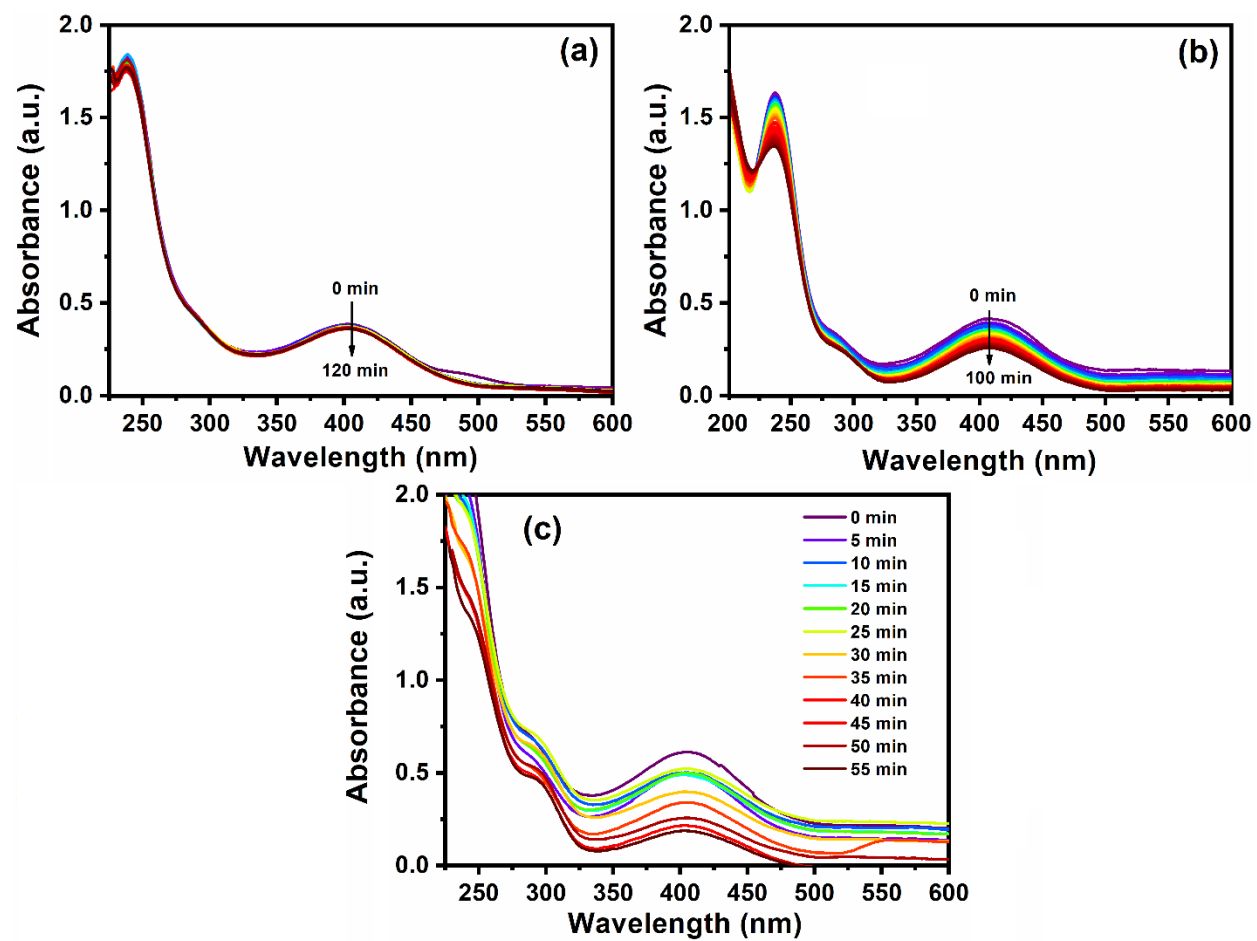


**Fig. S33.** UV-Vis absorption spectra for the photodegradation of ROX in the (a) absence of VL, (b) GCN, and (c) NiCo-P catalysts.

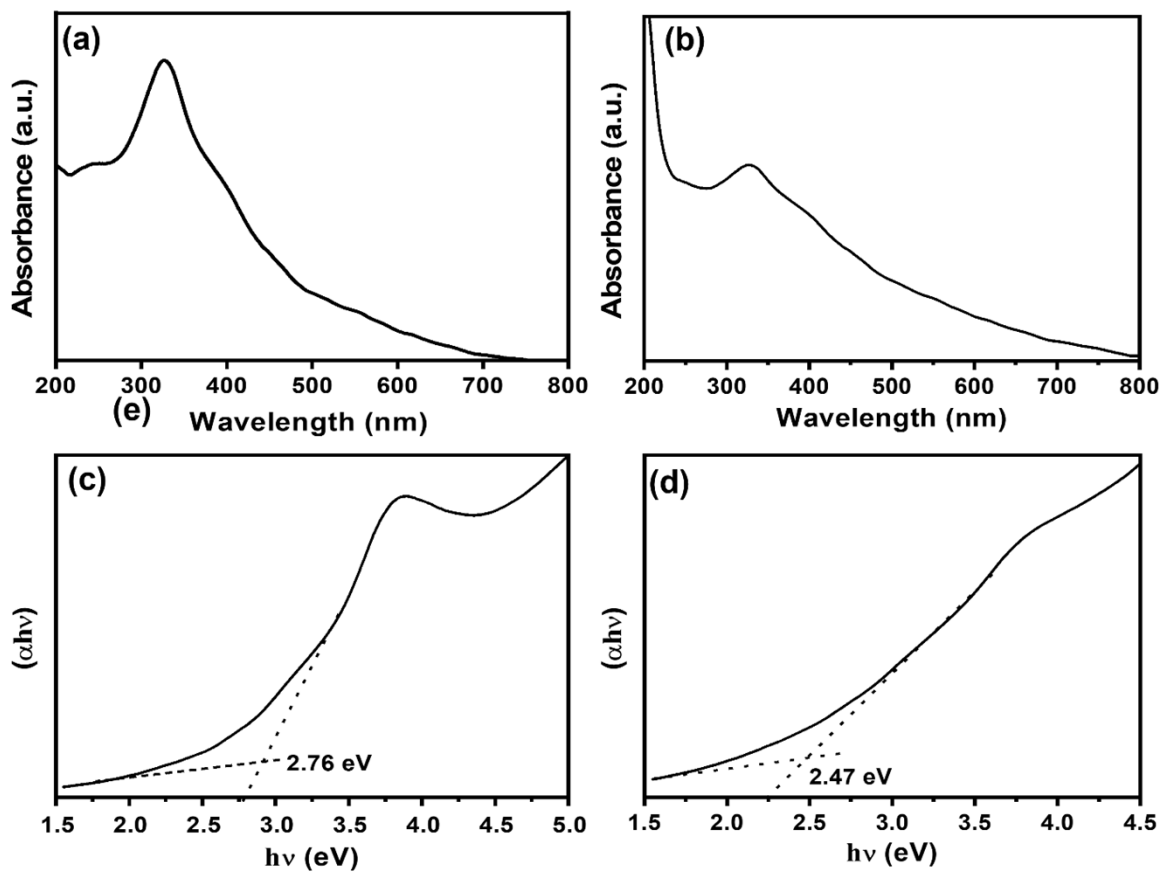


**Fig. S34.** (a,b) UV spectra and (c,d) Tauc plots of GCN and CrNiCo-P/GCN.

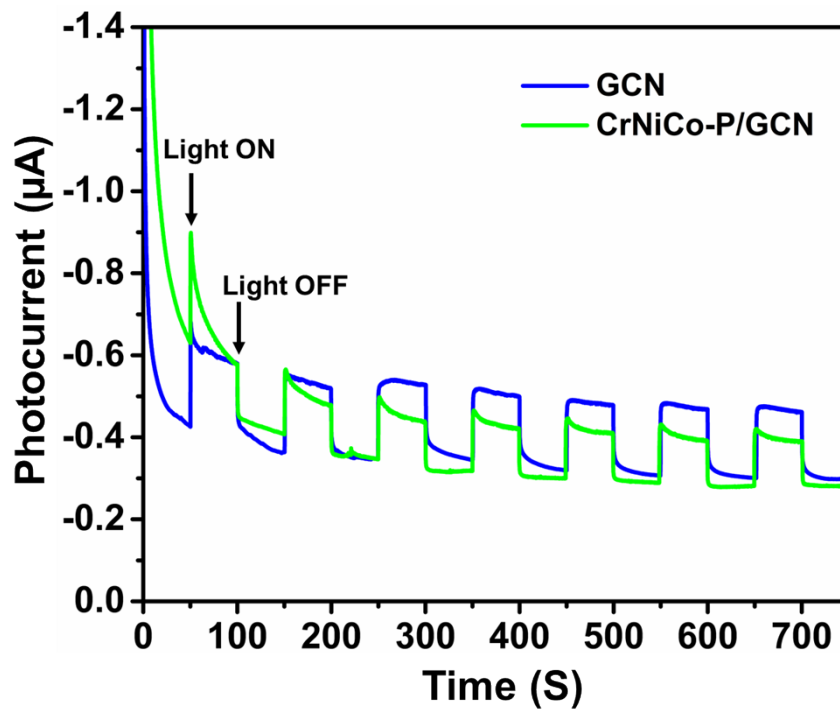


**Fig. S35.** Photocurrent measurement of GCN and CrNiCo-P/GCN in 0.1 M NaOH under the UV light wavelength of 365 nm.

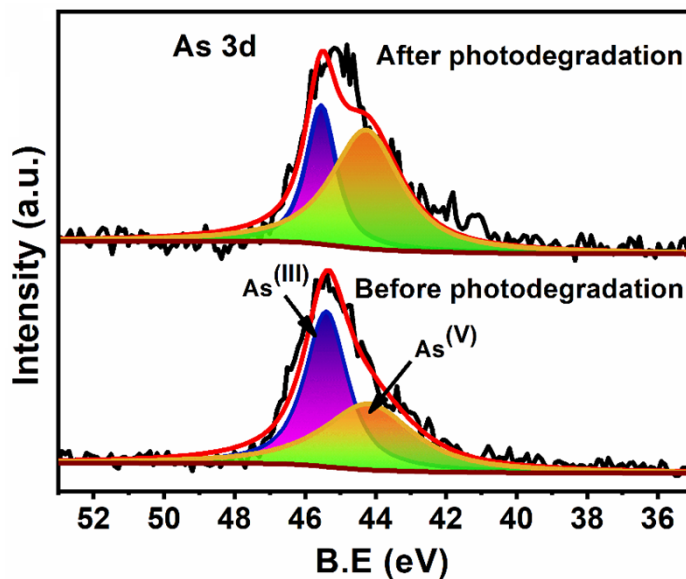


**Fig. S36.** The XPS high-resolution spectra of As 3d before photodegradation, and after photodegradation of ROX in the presence of CrNiCo-P/GCN.

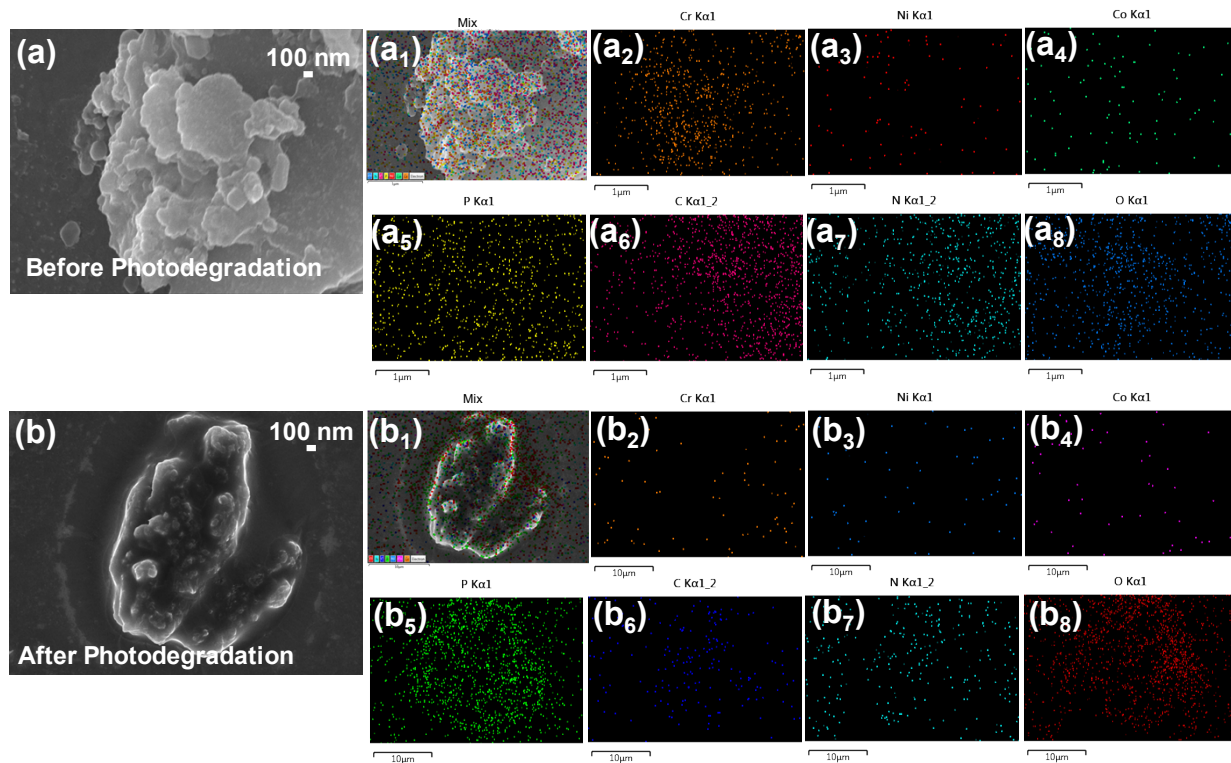


**Fig. S37.** The FE-SEM images of CrNiCo-P/GCN: (a) Before photodegradation stability material of ROX with corresponding FE-SEM-EDX elemental mapping of (a<sub>1</sub>-a<sub>8</sub>) Mix, Cr, Ni, Co, P, C, N, and O. (b) After photodegradation stability material of ROX with corresponding FE-SEM-EDX elemental mapping of (b<sub>1</sub>-b<sub>8</sub>) Mix, Cr, Ni, Co, P, C, N, and O.

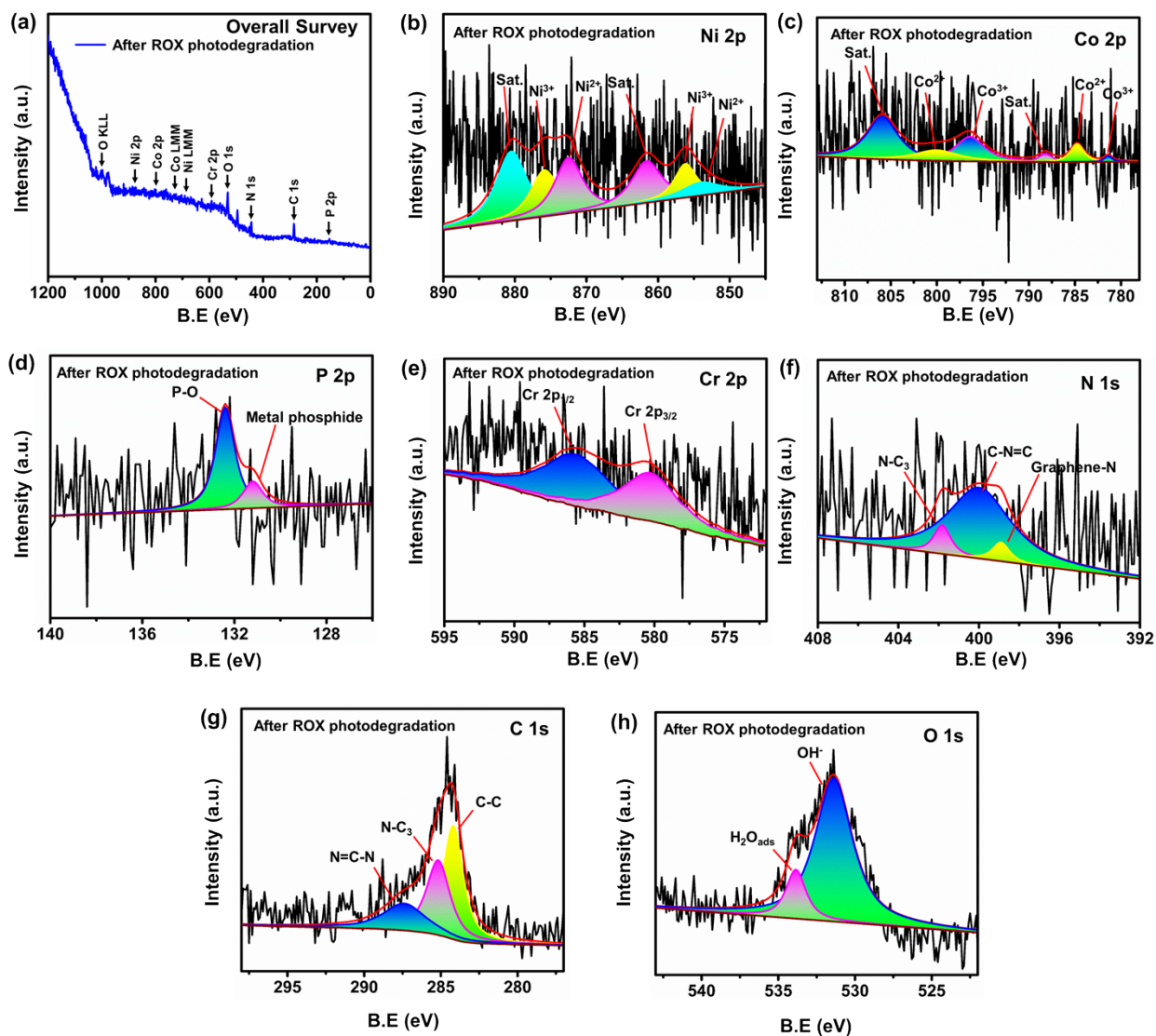


**Fig. S38.** XPS spectrum of before and after ROX photodegradation stability of CrNiCo-P/GCN: (a) overall survey, and high-resolution of (b) Ni 2p, (c) Co 2p, (d) P 2p, (e) Cr 2p, (f) N 1s, (g) C 1s, (h) O 1s.

Note: The resultant sample was coated in ITO glass for XPS measurement so it may be slightly different from the original.



**Table S1.** Summary of textural properties of prepared samples

Samples	textural properties		
	$S_{\text{BET}}^a$ ( $\text{m}^2 \text{g}^{-1}$ )	$V_{\text{tot}}^a$ ( $\text{cm}^3 \text{g}^{-1}$ )	$D_p^b$ (nm)
GCN	62.29	0.0082	1.18
CrNiCo-P/GCN	43.27	0.0031	1.12

<sup>a</sup>BET surface area,  $S_{\text{BET}}$ , and pore volume,  $V_{\text{tot}}$ , derived at  $P/P_0 = 0.99$ . <sup>b</sup>Pore diameter,  $D_p$ , calculated by the Barrett–Joyner–Halenda (BJH) method using adsorption branches of isotherms.

**Table S2.** Elemental quantitative results of CrNiCo-P/GCN from HRTEM-EDS.

Elements	Weight%
Cr K	7.98
Ni K	30.08
Co K	4.85
P K	4.44
C K	37.38
N K	1.27
Total	100

**Table S3.** Elemental results for CrNiCo-P/GCN, CrNiCo-P, NiCo-P, and GCN derived from surface sensitive XPS.

Samples	Ni 2p (%)	Co 2p (%)	P 2p (%)	Cr 2p (%)	N 1s (%)	C 1s (%)
CrNiCo-P/GCN	36.96	8.13	4.66	1.95	1.61	46.69
CrNiCo-P	76.60	13.51	6.65	3.33	–	–
NiCo-P	52.13	21.86	26.01	–	–	–
GCN	–	–	–	–	2.79	97.21

**Table S4.** Summary of various catalytic electrodes for OER in 1.0 M KOH.

<b>Electrocatalysts</b>	<b>OER (j=10 mA cm<sup>-2</sup>, mV)</b>	<b>ref.</b>
NiCo-NiCoO <sub>2</sub> @NC <sup>a</sup>	318	S2
NiCo <sub>2</sub> O <sub>3</sub> @OMC <sup>b</sup>	281	S3
Mo <sub>2</sub> C@CS <sup>c</sup>	320	S4
Ni <sub>0.75</sub> Fe <sub>0.25</sub> -N, P, S/C	290	S5
CoP/rGO	340	S6
PO <sup>d</sup> -Ni/Ni-N-CNTs	420	S7
Fe-Ni@NC-CNTs	274	S8
NiCoFeP	273	S9
NiO	405	S10
CoP/C	330	S11
NiCoP/NC <sup>a</sup> PHCs <sup>e</sup>	297	S12
CrNiCo-P	330	This work
CrNiCo-P/GCN	290	This work

<sup>a</sup>N-doped Carbon. <sup>b</sup>Ordered Mesoporous Carbon. <sup>c</sup>Carbon Sheet. <sup>d</sup>Partially Oxidized. <sup>e</sup>Polyhedral Nanocages.

**Table S5.** The Turn Over Frequencies (TOFs) values of synthesized catalysts for OER (at J = 10 mA cm<sup>-1</sup>)

<b>Catalysts</b>	<b>TOFs value (s<sup>-1</sup>)</b>
CrCo-P	0.012
CrCo-P/GCN	0.020
CrNi-P	0.041
CrNi-P/GCN	0.103
NiCo-P	0.042
NiCo-P/GCN	0.094
CrNiCo-P	0.029
CrNiCo-P/GCN	0.889

**Table S7.** Comparison of CrNiCo-P/GCN modified electrode to the previously reported literatures for electrochemical detection of ROX.

Modified Catalyst	Method	Electrolyte/ pH	WLR ( $\mu\text{M}$ )	LOD ( $\mu\text{M}$ )	Sensitivity ( $\mu\text{A } \mu\text{M}^{-1}$ $\text{cm}^{-2}$ )	ref.
MCPME <sup>a</sup>	DPV	0.04 M BRB/2.0	2–100	0.53	–	S13
SrWO <sub>4</sub> NPs <sup>b</sup> /GrO <sup>c</sup> /GCE	AM <sup>i</sup>	0.1 M PB/7.0	0.035– 1816.5	0.0225	9.985	S14
WS <sub>2</sub> NRs <sup>d</sup> /N- rGOs <sup>e</sup> /SPCE <sup>f</sup>	DPV	0.05 M PB/7.0	0.1–442.6	0.075	14.733	S15
WS <sub>2</sub> NSs <sup>g</sup> /SPCE <sup>f</sup>	DPV	0.05 M PB /7.0	0.05–490	0.030	28.966	S16
CoMn <sub>2</sub> O <sub>4</sub> -500/SPCE <sup>f</sup>	DPV	0.05 M PB/7.0	0.01- 0.84;0.84- 1130	0.002	33.13	S17
La <sub>2</sub> (MoO <sub>4</sub> ) <sub>3</sub> /SPCE <sup>f</sup>	DPV	0.05 M PB/7.0	0.025-2650	0.0124	13.366 & 42.619	S18

Tm-BTC MOF/GCE	DPV	0.1 M PB/7.0	0.00015-770	0.0001	-	S19
CrNiCo-P/GCN/GCE	DPV	0.1 M PB/5.0	0.001–0.413 mM	0.031	1.7619 $\mu\text{A}$ mM <sup>-1</sup> cm <sup>2</sup>	This work

<sup>a</sup>Modified carbon paste microelectrode. <sup>b</sup>Strontium tungstate. <sup>c</sup>Graphene oxide. <sup>d</sup>Tungsten sulfide nanorods. <sup>e</sup>Nitrogen doped reduced graphene oxides. <sup>f</sup>Screen printed carbon electrode. <sup>g</sup>Tungsten disulfide nanosheets. <sup>h</sup>Thulium Metal. <sup>i</sup>Amperometry. <sup>j</sup>Britton–Robinson buffer.

**Table S8.** Voltammetric determination of ROX in chicken and swine meat samples.

Meat sample		Spiked (mM)	Found (mM)	Recovery (%)	RSD*
Chicken	unrealized	0.001	0.00	–	–
	realized	0.001	0.00098	98.0	±0.061
	realized	0.003	0.0029	99.5	±0.047
Swine	unrealized	0.001	0.00	–	–
	realized	0.001	0.00097	97.5	±0.082
	realized	0.003	0.0029	99.5	±0.095

\*Measurement of three experiments (n = 3) and presented the best data Fig. only.

**Table S9.** Chemical structure and some properties of ROX used in this study

Common name	Roxarsone (ROX)
IUPAC name	(4-hydroxy-3-nitrophenyl)arsonic acid
Synonyms	3-Nitro-4-hydroxyphenylarsonic acid; Nitrophenolarsonic acid; 4-Hydroxy-3-nitrophenylarsonic acid; 4-Hydroxy-3-nitrobenzenearsonic acid; 2-Nitro-1-hydroxybenzene-4-arsonic acid; (4-Hydroxy-3-nitrophenyl)arsonic acid;
Appearance	Tufts of pale-yellow needles or rhombohedral plates
Empirical formula	$C_6H_6AsNO_6$
Melting point	>300 °C (572 °F; 573 K)
Solubility in water (mg L <sup>-1</sup> )	less than 1 mg at 23 °C (72 °F)
Solubility in other solvents	Slightly sol in cold water; freely sol in methanol, ethanol, acetic acid, acetone, alkalies; sol in about 30 parts boiling water; insol in ether, ethyl acetate; sparingly sol in dil mineral acids
Molecular weight (g mol <sup>-1</sup> )	263.04
Stabililty	Stable under ordinary conditions (light sensitive)
Chemical Class	Organoarsonic acid
Toxicity	Oral rat LD50; 81mg/kg
Applications	4-Hydroxy-3-nitrobenzenearsonic acid, an arsenic derivative, is used in veterinary medicine to promote growth, feed efficiency and pigmentation and to control swine dysentery. It is used as a synergist of primary anticoccidials which treat or inhibit the growth of coccidiosis in animals or in man.

Molecular structure

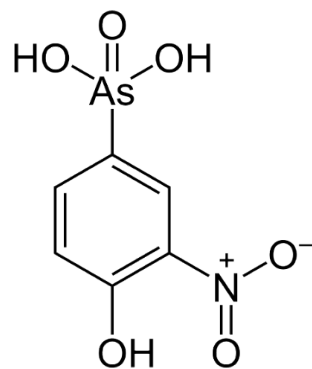


**Table S10.** Photodegradation performances of ROX over various catalysts

Photocatalyst	Catalyst (mg)	ROX (mg L <sup>-1</sup> )	pH	Time (min)	Source	Ref.
$\alpha$ -FeOOH@GCA <sup>a</sup>	50	20	3.58	120	Hp lamp	[S20]
ZnO	2500	15	7.0	180	UV lamp	[S21]
Bi <sub>0.5</sub> Fe <sub>0.5</sub> VO <sub>4</sub> /SCN <sup>b</sup>	50	50	7.5	90	Hg-Xe lamp	[S22]
TiO <sub>2</sub> /FeOOH	100	10	7.0	120	UV lamp	[S23]
CrNiCo-P/GCN	10	0.01	7.0	70	Xe lamp	This work

<sup>a</sup>Reduced graphene oxide and carbon nanotubes aerogel. <sup>b</sup>Sulfur doped graphitic carbon nitride.

## References

- (S1) K. Karthick, S. Anantharaj, P. E. Karthik, B. Subramanian, S. Kundu, *Inorg. Chem.* 2017, **56** (11), 6734–6745.
- (S2) Y. Xiao, P. Zhang, X. Zhang, X. Dai, Y. Ma, Y. Wang, Y. Jiang, M. Liu, Y. Wang, *J. Mater. Chem. A* 2017, **5** (30), 15901–15912.
- (S3) Y. Zhang, X. Wang, F. Luo, Y. Tan, L. Zeng, B. Fang, A. Liu, *Appl. Catal. B Environ.* 2019, **256**, 117852.

- (S4) H. Wang, Y. Cao, C. Sun, G. Zou, J. Huang, X. Kuai, J. Zhao, L. Gao, *ChemSusChem* 2017, **10** (18), 3540–3546.
- (S5) J. Wang, Y. Gao, T. L. You, F. Ciucci, *J. Power Sources* 2018, **401**, 312–321.
- (S6) L. Jiao, Y. X. Zhou, H. L. Jiang, *Chem. Sci.* 2016, **7** (3), 1690–1695.
- (S7) Z. Y. Wu, W. B. Ji, B. C. Hu, H. W. Liang, X. X. Xu, Z. L. Yu, B. Y. Li, S. H. Yu, *Nano Energy* 2018, **51**, 286–293.
- (S8) C. Gu, S. Hu, X. Zheng, M. R. Gao, Y. R. Zheng, L. Shi, Q. Gao, X. Zheng, W. Chu, H. B. Yao, J. Zhu, S. H. Yu, *Angew. Chemie* 2018, **130** (15), 4084–4088.
- (S9) Y. Guo, J. Tang, Z. Wang, Y. Sugahara, Y. Yamauchi, *Small* 2018, **14** (44), 1–8.
- (S10) J. Zheng, W. Zhou, T. Liu, S. Liu, C. Wang, L. Guo, *Nanoscale* 2017, **9** (13), 4409–4418.
- (S11) Y. Bai, H. Zhang, Y. Feng, L. Fang, Y. Wang, *J. Mater. Chem. A* 2016, **4** (23), 9072–9079.
- (S12) X. Zhang, L. Huang, Q. Wang, S. Dong, *J. Mater. Chem. A* 2017, **5** (35), 18839–18844.
- (S13) M. Waris, J. A. Baig, Sirajuddi, T. G. Kazi, I. B. Solangi, S. Siddiqui, H. I. Afridi, *Food Anal. Methods* 2016, **9** (8), 2142–2151.
- (S14) M. Govindasamy, U. Rajaji, S. F. Wang, Y. J. Chang, R. J. Ramalingam, C. Y. Chan, *J. Taiwan Inst. Chem. Eng.* 2020, **114**, 211–219.
- (S15) T. W. Chen, U. Rajaji, S. M. Chen, S. Chinnapaiyan, R. Ramalingam, *J. Ultrason. Sonochem.* 2019, **56**, 430–436.
- (S16) M. Govindasamy, S. F. Wang, R. Jothiramalingam, S. Noora Ibrahim, H. A. A. Al-lohedan, *Microchim. Acta* 2019, **186** (7).
- (S17) T. Kokulnathan, V. Rajagopal, T. J. Wang, S. J. Huang, F. Ahmed, *Inorg. Chem.* 2021, **60** (23), 17986–17996.
- (S18) S. Vinoth, M. Govindasamy, S. F. Wang, A. A. Alothman, R. A. Alshgari, *Microchem. J.* 2021, **164**, 106044.
- (S19) S. Chinnapaiyan, U. Rajaji, S. M. Chen, T. Y. Liu, J. I. de Oliveira Filho, Y. S. Chang, Y. S. *Electrochim. Acta* 2022, **401**, 139487.
- (S20) S. Su, C. Cao, Y. Zhao, D. D. Dionysiou, *Appl. Catal. B Environ.* 2019, **245**, 207–219.

- (S21) K. Acuña, J. Yáñez, S. Ranganathan, E. Ramírez, J. Pablo Cuevas, H. D. Mansilla, P. Santander, *Sol. Energy* 2017, **157**, 335–341.
- (S22) S. Balu, Y. L. Chen, S. W. Chen, T. C. K. Yang, *Appl. Catal. B Environ.* 2022, **304** (1), 120852.
- (S23) W. Fu, D. L. Lu, H. Yao, S. Yuan, W. Wang, M. Gong, Z. H. Hu, *Environ. Sci. Pollut. Res.* 2020, **27** (15), 18434–18442.